Petroleum Science 21 (2024) 4230–4247

Contents lists available at ScienceDirect

Petroleum Science

journal homepage: www.keaipublishing.com/en/journals/petroleum-science

Original Paper

Multi-fracture growth behavior during TPDF in a horizontal well of multi-clustered perforations: An experimental research

Yu-Shi Zou [a, *], Can Yang [a], Shi-Cheng Zhang [a], Xin-Fang Ma [a], Yan-Chao Li [b], Long-Qing Zou [b]

[a] State Key Laboratory of Petroleum Resources and Engineering, China University of Petroleum (Beijing), Beijing, 102249, China
[b] Shale Gas E&D Project Department, CNPC Chuanqing Drilling Engineering Co., Ltd., Chengdu, 610052, Sichuan, China

ARTICLE INFO

Article history:
Received 18 March 2024
Received in revised form
14 August 2024
Accepted 15 August 2024
Available online 21 August 2024

Edited by Yan-Hua Sun

Keywords:
Shale
Temporary plugging and diverting fracturing
Bedding planes
Natural fractures
Multiple fractures

ABSTRACT

Temporary plugging and diverting fracturing (TPDF), involving inner-fracture temporary plugging (IFTP) and inner-stage temporary plugging (ISTP), has been proposed as a widely applied technique in China, for promoting the uniform initiation and propagation of multi-clustered hydraulic fractures (HFs) in a horizontal well of the shale oil/gas reservoirs. However, how the key plugging parameters controlling the multi-fracture growth and the pumping pressure response during TPDF in shale with dense bedding planes (BPs) and natural fractures (NFs) is still unclear, which limits the optimization of TPDF scheme. In this paper, a series of TPDF simulation experiments within a stage of multi-cluster in a horizontal well were carried out on outcrops of Longmaxi Formation shale using a large-scale true tri-axial fracturing simulation system, combined with the acoustic emission (AE) monitor and computed tomography (CT) scanning techniques. Each experiment was divided into three stages, including the conventional fracturing (CF), IFTP and ISTP. Multi-fracture initiation and propagation behavior, and the dominant controlling parameters were examined, containing the particle sizes, concentration of temporary plugging agent (TPA), and cluster number. The results showed that the number of transverse HFs (THFs) and the overall complexity of fracture morphology increase with the increase in TPA concentration and perforation cluster number. Obviously, the required concentration of TPA is positively correlated with the cluster number. Higher peak values and continuous fluctuations of pumping pressure during TPDF may indicate the creation of diversion fractures. The creation of standard THFs during CF is favorable to the creation of diversion fractures during TPDF. Moreover, the activation of BPs nearby the wellbore during CF is unfavorable to the subsequent pressure buildup during TPDF, resulting in poor plugging and diverting effect. Notably, under the strike-slip fault stress regime, the diversion of THFs is not likely during IFTP, which is similar as the results of ISTP to initiate mainly the un-initiated or under-propagated perforation clusters. Three typical pressure curve types during TPDF can be summarized to briefly identify the hydraulic fracture diversion effects, including good (multiple branches or/and THFs can be newly created), fair (HF initiation along the slightly opened BPs and then activating the NFs), and bad (HF initiation along the largely opened BPs and then connecting with the NFs).

1. Introduction

Multiple closely spaced hydraulic fractures (HFs) in a horizontal well are expected to be created to help achieve the economic development of unconventional shale resources. However, shale reservoirs may exhibit heterogeneity along the horizontal wellbore, resulting in the differences in breakdown pressure among different perforation clusters (King, 2010; Bai et al., 2020; Daneshy, 2020; Dontsov and Suarez-Rivera, 2020; Duan et al., 2020; Snyder et al., 2021), as well as the fracture propagation (Tan et al., 2023; Yang et al., 2023; Lei et al., 2024) and conductivity (Wang L. et al., 2022). Nevertheless, strong stress interference among multiple HFs with tight spacing can cause nonuniform simultaneous propagation or asymmetrical propagation of subsequent HFs (Olson, 2008; Lecampion and Desroches, 2015; Salimzadeh et al., 2017; Manchanda et al., 2018; Zhang Z.P. et al., 2021; Lu and He, 2022;

* Corresponding author.
E-mail address: zouyushi@126.com (Y.-S. Zou).

https://doi.org/10.1016/j.petsci.2024.08.003

Wang W.R. et al., 2022; Yu et al., 2022; Zhu et al., 2023). Meanwhile, the complexity of HF created is generally insufficient in the formations with features such as high horizontal differential stress or/and low density of natural fractures (Zou et al., 2016a, 2016b; Ali et al., 2016, 2017; Xie et al., 2018; Qin et al., 2023). To address abovementioned issues, one promising technology, termed "inner-fracture or/and inner-stage" temporary plugging and diverting fracturing (TPDF), has been proposed and advanced continuously. It is of great important to understand the mechanism of HF diversion to optimize the operation scheme and key parameters of such technology.

To date, many laboratory experiments and theoretical research have been carried out to study the pattern of multi-fracture growth during TPDF. Many influence factors may contribute to the effect of TPDF, including horizontal differential stress, inhomogeneity (e.g., stress or rock strength variation, existence of geological discontinuities), types and particle sizes of temporary plugging agent, pumping rate, and fluid viscosity, etc. (Wang et al., 2017; Zhang et al., 2019; Zou et al., 2020; Chen et al., 2020; Yuan et al., 2020; Li et al., 2022; Shi et al., 2022; Wang L. et al., 2022; Zou et al., 2024). Zou et al. (2020) pointed out that horizontal differential stress is the most influential geological parameter that governs the growth behavior of HFs during the inner-fracture TPDF. For a moderate horizontal differential stress of 8 MPa, the growth of a single planar HF before plugging can be changed into a complex HF network through opening of natural fractures (NFs) after plugging. However, for a high horizontal differential stress of 12 MPa, it is difficult to achieve the HF diversion by opening the NFs during the inner-fracture TPDF. Chen et al. (2020) found that stress difference among multi-clustered perforations is a critical parameter for HF diversion during the inner-stage TPDF in a horizontal well. More ball sealers and earlier plugging time are required to promote the uniform growth of multiple fractures under the condition of higher stress difference among multi-clustered perforations. Tang et al. (2023) suggested that the timing of plugging is influenced by NFs. The higher the density of NFs or the lower the orientation of NFs, the later the timing of plugging should be. Wang et al. (2021) carried out true tri-axial fracturing experiments to study the TPDF in a vertical well and found that when plugging occurs at the fracture tip, the HF may grow along the direction perpendicular to the primary fracture, but the overall diversion effect is not obvious in the real three-dimensional fracture; when plugging occurs at the middle of a fracture, it is easier to obtain an S-shaped fracture (Fig. 1). Zhang et al. (2020) indicated that the most influential engineering parameter to govern such plugging location and diverting fracture propagation mode is the concentration of temporary plugging agent (TPA). Zou et al. (2024) suggested that with the increase in TPA concentration, the peak pressure first rises and then decreases. Comprehensive CT scans of the distribution of TPA within fractures and segments of post-fracturing samples revealed that excessive amounts of the TPA may lead to ineffective plugging. To sum up, several experimental simulations of TPDF in the wellbore with open-hole completion have been performed (Zhang et al., 2019; Zhang et al., 2020; Wang B. et al., 2020; Guo et al., 2020), but few have been involved in the simulation of multi-cluster fracturing in a horizontal well. How the particle sizes and concentration of TPA affect the fracture diversion have yet not been clarified. Moreover, the roles of dense bedding planes (BPs) during TPDF in shale are still unclear.

Therefore, in this study, a series of "inner-fracture + inner-stage" TPDF simulation experiments were performed on outcrops of Longmaxi Formation shale under the triaxial stresses. The intention of inner-fracture temporary plugging (IFTP) is to create a high-strength plug at the tip of a fracture, causing the stress field at the fracture tip to divert the fracture, while inner-stage temporary plugging (ISTP) is to plug the opened clusters to increase the wellbore pressure, inducing fractures in unopened clusters and improving the equal distribution of stimulation across each perforation cluster. One fracturing stage of multi-cluster in a horizontal well with casing completion was designed uniquely. The overall process, including initiation, propagation, and diversion of HFs in a horizontal well has been explored by the acoustic emission (AE) monitor, combined with the CT scanning. The number of clusters, particle sizes, and concentration of TPA were examined in detail. The findings can provide a theoretical basis for the optimization of engineering parameters of TPDF in a horizontal well of multi-clustered perforations in shale with dense BPs or/and NFs.

2. Experimental methods

2.1. Rock physical properties

Outcrop of the Longmaxi Formation shale in the Sichuan Basin, China was mined from an underground pit (about 100 m below surface). Given that it is preserved in such condition where weathering is very limited, the specimens prepared from the outcrop have similar mineral compositions and physical properties as those of the cores collected from downhole. X-ray diffraction results show that the mineral compositions of the specimen include 50.9% quartz, 10.1% carbonatite, 33% clay, and 6% pyrite (by weight). Table 1 exhibits several main petrophysical parameters of the specimen used, including the rock porosity, permeability (under the effective confining pressure of 5 MPa), and mechanical parameters. It is noted that the shale samples used have significant anisotropy characteristics. That is, two sets of distinct parameter values are exhibited in the directions parallel to and perpendicular

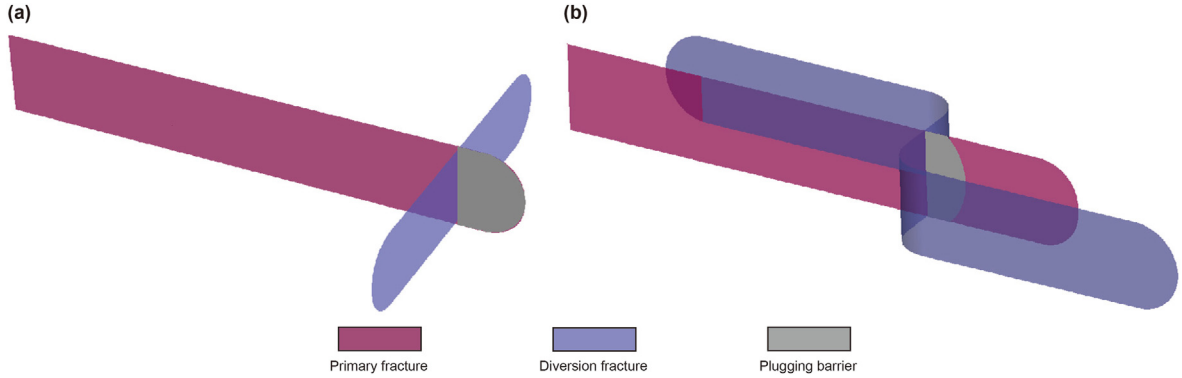

Fig. 1. Diversion fracture morphology of different plugging locations. (**a**) Plugging occurs at the fracture tip; (**b**) Plugging occurs at the middle of the fracture.

Table 1
Rock petrophysical parameters of different core drilling directions.

Core drilling direction	Porosity, %	Permeability, 10^{-18} m^2	Young's modulus, GPa	Poisson's ratio	Compression strength, MPa	Tensile strength, MPa
Perpendicular to BPs	4.42	0.015	41.6	0.269	257.2	8.85
Parallel to BPs	4.42	0.232	52.3	0.245	203.1	6.92
Along the NFs	/	1.22–10.63	/	/	/	4.2–7.6

to the BPs. As a result, different fracture morphologies for the different core drilling directions were present after the triaxial compression tests. The presence of dense BPs and NFs, as the mechanical weak planes, have potential impact on the HF propagation path and complexity. Meanwhile, due to the existence of calcite-filled NF along the central axis of the core, the tensile strength is relatively low compared with the cores without NFs.

2.2. Specimen preparation and experimental scheme

To match the fracturing simulation system and ensure sufficient fracture propagation space, large shale outcrops of several meters long were cut into several cubic blocks of 30 cm × 30 cm × 30 cm by using a large-scale stone cutter, as shown in Fig. 2(a). A total of 21 cubic block specimens were prepared in this study. Before the fracturing experiments, CT scanning was carried out to recognize the distribution of slightly opened BPs and NFs within the specimens (Fig. 2(b) and (c)).

Fig. 3(a) and (b) show the simulation method of casing perforation in a horizontal wellbore. A hole with a depth of 25 cm was drilled along the BPs at the surface center of the cubic block by a special coring bit with an outer diameter of 3 cm and a length of 27 cm. And a polyvinyl chloride (PVC) pipe with an outer diameter of 2.5 cm, an inner diameter of 2.2 cm and a length of 25 cm was bonded to the borehole with epoxy to simulate the casing and cementing processes. The surface of the PVC casing should be grooved to increase the roughness to enhance the bonding strength between the PVC casing and rock wall surface (Fig. 3(c)). After that, 3 to 9 circle notches with a depth of 0.3 cm and a width of 3 mm were cut inside the wellbore orthogonal to the axis of the PVC pipe by a notch-cutting machine to simulate the multiple clustered perforations. The spacing between notches was determined according to a geometric similarity criterion (Zhang S.C. et al., 2021; Zou et al., 2022):

$$\frac{S_E}{S_F} = \alpha \frac{L_E}{L_F} \tag{1}$$

where S is the notch spacing; L is the fracture length; α is the empirical parameter, $\alpha = 1.667$; subscripts E and F represent experimental parameters and field parameters, respectively. The half-length of the fracture is approximately 200 m in the field and 15 cm in the laboratory, respectively. The cluster spacing in the field is approximately 15 m. According to Eq. (1), the notch spacing is 2 cm. A stainless-steel injection tube with three built-in independent fluid injection pipelines was designed innovatively for the multi-stage and multi-cluster fracturing, as shown in Fig. 3(d) (Zhang S.C. et al., 2021; Zou et al., 2022), and the injection tube with a single fluid injection pipeline was used for the TPDF in a horizontal well of multi-cluster (Fig. 3(e)). The injection tube for multi-stage fracturing comprises an injection end with three injection ports and three fracturing stages separated by rubber seals, each containing an effluent hole. A specific injection port is connected to a corresponding effluent hole within each stage through internal tubing. Sequential injection of the fracturing fluid into the three injection ports facilitates staged fracturing (Fig. 3(f)). A total of 21 specimens from Longmaxi Formation were prepared by the above method. Specimen 0# was fractured using the injection tube for the fracturing with three stages, during which a relatively short stage spacing of 4 cm and only two clusters spaced 8 mm per stage were set. This experiment was considered as the control group. It can be used to simulate the precise fracturing mode in field. Then TPDF in a horizontal well of multi-cluster was carried out on specimens 1#-20# by using injection tube with a single fluid injection pipeline. For these 20 specimens, a relatively long stage spacing of 15 cm and 3, 5, 7 or 9 clusters were set.

According to one of the real in-situ triaxial stresses conditions of Longmaxi Formation shale (Zou et al., 2021; Li et al., 2018a, 2018b), the strike-slip fault stress regime (the maximum horizontal stress is

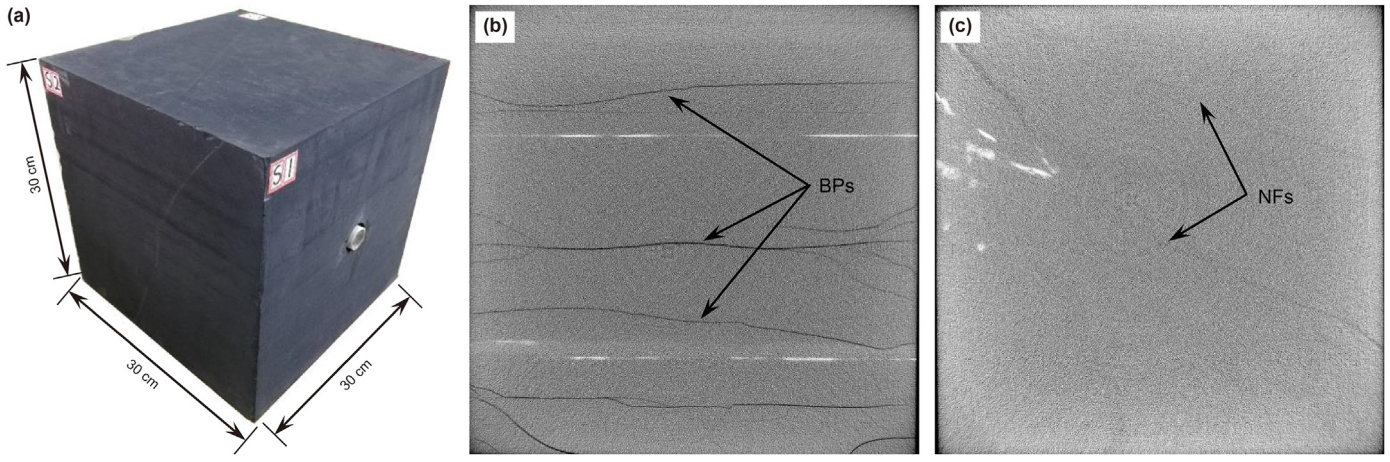

Fig. 2. Specimen prepared for fracturing experiment. (**a**) Cubic shale specimen; (**b**) CT scanning image identifying the slightly-opened BPs; (**c**) CT scanning image identifying the NFs.

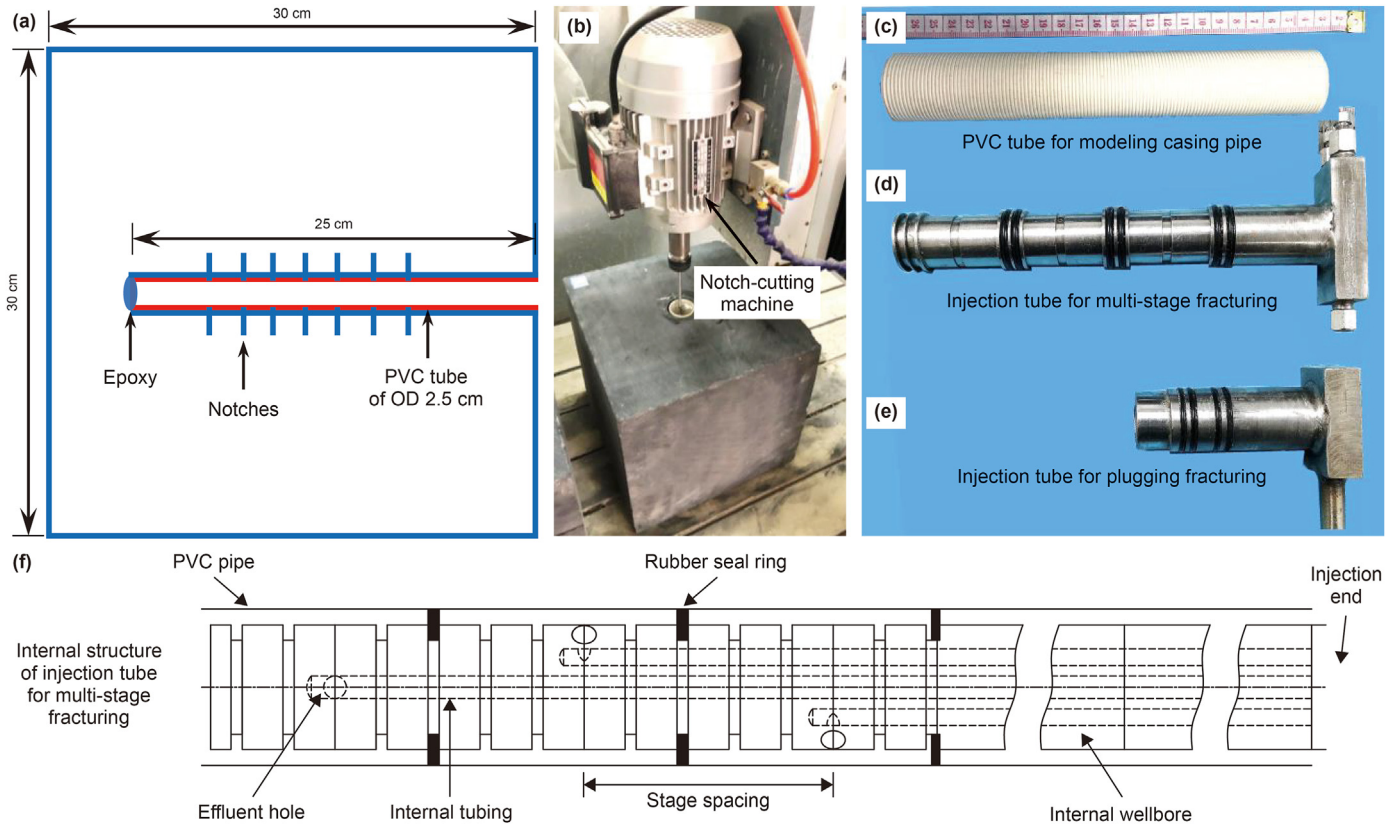

Fig. 3. Completion method and injection tubes. (**a**) Schematic diagram of completion in the horizontal wellbore; (**b**) Notch-cutting machine; (**c**) PVC tube for modeling casing pipe; (**d**) Injection tube for multi-stage fracturing, (**e**) Injection tube for plugging fracturing; (**f**) Internal structure of injection tube for multi-stage fracturing (modified from Liu et al., 2018).

higher than the vertical stress) was adopted in this study. Due to the limitations of apparatus, the relative triaxial stresses were applied to the specimens, that is the horizontal and vertical stress differences were 15 and 10 MPa, respectively. The maximum horizontal stress (σ_H), the minimum horizontal stress (σ_h), and the vertical stress (σ_V) applied on the cube specimens were set as 25, 10, and 20 MPa, respectively. The pumping rate in experiments was calculated according to similarity criterion (Zhang S.C. et al., 2021; Zou et al., 2022):

$$Q_E = \beta Q_F \frac{w_E h_E}{w_F h_F} \tag{2}$$

where Q is the pumping rate; w is the fracture width; h is the fracture height; β is the empirical parameter, $\beta = 1.1$.

In the field operation, the pumping rate, fracture width, and height are about 12–18 m^3/min, 6–10 mm, and 20–30 m, respectively. The fracture width and height in the laboratory are about 1 mm and 0.3 m, respectively. The calculated pumping rate in the laboratory is 200 mL/min. Slickwater of 2–5 mPa·s was used in all the specimens. It is noted that an independent experiment (specimen 0#) was designed and performed before the twenty TPDF experiments. In this experiment, three stages (spacing 4 cm) and two clusters (spacing 0.8 cm) per stage in a horizontal well were considered. It was used to illustrate the difficulty to create multiple HFs uniformly in a long stage of a horizontal well. Table 2 shows the detailed experimental scheme of the TPDF simulation for the twenty specimens. Specimens 1#–5# and 10#–20# were used to analyze the influence of the concentration of TPA and cluster number. Specimens 6#–9# were used to study the effect of the particle size of TPA on fracture morphology by choosing four sizes of TPA, i.e., 200/300 mesh (48–75 μm), 100 mesh (150 μm), 20/70 mesh (212–830 μm), and 1–2 mm, as shown in Fig. 4(a). Based on previous experimental experience, the TPAs with these particle sizes can effectively form plugging zones at the HF mouth and within the HF under the specified experimental fracture width and notch width. The TPAs used are identical to those used in field applications and exhibit excellent material properties. It is noted that the TPA has good suspension mixed in the fracturing fluid, which indicates that it has good transport capacity inside the fracture, as shown in Fig. 4(b). Note that the combination of two particle sizes of TPA was used generally for each plugging stage, as shown in Table 2.

2.3. Experimental instruments and procedures

Experiments were performed through a large-scale true tri-axial fracturing simulation system (Li et al., 2017; Zou et al., 2021). It is consisted of a cubic specimen chamber, an oil-pressure pump package, a constant pressure and speed duplex pump, intermediate containers, a sand adding device, a data acquisition system, and auxiliary equipment, etc. (Fig. 5). An AE monitoring system (DS-5) with 32 channels was applied to explore the rock broken mechanism during the experiments.

Each experiment was divided into three stages, including the conventional fracturing (CF), IFTP, and ISTP. Firstly, HFs were created by the CF. Secondly, TPA of smaller sizes was pumped with slickwater to plug the tips of HFs. As the pressure continuing to increase, the diversion fractures or branches were created. Thirdly, TPA of larger sizes was then pumped to plug the entrances of

Table 2
Scheme of TPDF experiments.

Specimen No.	Specimen features	Cluster number	Parameters of plugging agent for IFTP			Parameters of plugging agent for ISTP		
			Particle size, mm	Amount, g	Concentration, g/L	Particle size, mm	Amount, g	Concentration, g/L
1#	Dense horizontal BPs and two group of NFs of high dip angles	3	0.15 0.212–0.83	60 60	60	0.212–0.83 1–2	60 20	40
2#	Dense horizontal BPs and one group of NFs of low dip angle	3	0.15 0.212–0.83	60 20	40	0.212–0.83 1–2	40 20	30
3#	Dense horizontal BPs and two groups of NFs of high dip angles	5	0.15 0.212–0.83	60 20	40	0.212–0.83 1–2	40 20	30
4#	Dense slightly oblique BPs and two groups of NFs of low dip angels	5	0.15 0.212–0.83	80 40	60	0.212–0.83 1–2	60 40	50
5#	Dense horizontal BPs	5	0.15 0.212–0.83	100 60	80	0.212–0.83 1–2	80 60	70
6#	Dense horizontal BPs and one NF of high dip angle	7	0.048–0.075 0.212–0.83	60 20	40	0.212–0.83 1–2	40 20	30
7#	Dense slightly oblique BPs and one group of NFs of low dip angles	7	0.048–0.075 0.15	60 20	40	0.048–0.075 0.15	40 20	30
8#	Dense horizontal BPs	7	0.15 0.212–0.83	60 20	40	0.212–0.83 1–2	40 20	30
9#	Dense horizontal BPs	7	0.15 0.212–0.83	60 20	40	0.15 0.212–0.83 1–2	20 20 20	30
10#	Dense horizontal BPs and two group of NFs of high dip angles	7	0.15 0.212–0.83	60 60	60	0.212–0.83 1–2	40 20	30
11#	Dense horizontal BPs	7	0.15 0.212–0.83	70 50	60	0.212–0.83 1–2	40 20	30
12#	Dense horizontal BPs	7	0.15 0.212–0.83	80 40	60	0.212–0.83 1–2	60 40	50
13#	Dense horizontal BPs	7	0.15 0.212–0.83	100 60	80	0.212–0.83 1–2	80 60	70
14#	Dense horizontal BPs and one NF of high dip angle	7	0.15 0.212–0.83	120 80	100	0.212–0.83 1–2	90 70	80
15#	Dense horizontal BPs and one group of NFs of high dip angle	7	0.15 0.212–0.83	140 100	120	0.212–0.83 1–2	100 80	90
16#	Dense slightly oblique BPs and one group of NFs of low dip angle	9	0.15 0.212–0.83	60 20	40	0.212–0.83 1–2	40 20	30
17#	Dense horizontal BPs and two group of NFs of high dip angles	9	0.15 0.212–0.83	80 40	60	0.212–0.83 1–2	60 40	50
18#	Dense horizontal BPs	9	0.15 0.212–0.83	100 60	80	0.212–0.83 1–2	80 60	70
19#	Dense horizontal BPs	9	0.15 0.212–0.83	100 100	100	0.212–0.83 1–2	100 80	90
20#	Dense horizontal BPs	9	0.15	160	140	0.212–0.83	120	110

preferential HFs, so as to stimulate the uninitiated clusters or insufficient growing fractures. The specific experimental procedures for TPDF are as follows.

(1) **Stress loading.** Each specimen was placed in the cubic pressurization chamber with the wellbore oriented horizontally in the *x*-direction. Triaxial stresses, namely, minimum (σ_h), maximum (σ_H) horizontal and vertical (σ_v), stresses in the *X*-, *Y*-, and *Z*-axis directions, were loaded onto the specimen independently through an oil-pressure pump package, respectively (Ma et al., 2017; Zou et al., 2017).

(2) **Fluid pumping and TPA adding.** Slickwater was stored in the three intermediate containers and was mixed with three different color fluorescent agents, respectively, which were utilized as the tracers to distinguish the HFs created in the three stages (CF, IFTP, and ISTP) in each specimen. Two types of TPA were added to the two tanks (tanks 1 and 2) of the airtight sand mixer. Smaller size TPA in tank 1 and larger size TPA in tank 2 were used for the IFTP and the ISTP, respectively. During the CF stage, slickwater stored in the container C1 was pumped into the wellbore at a constant flow rate. Meantime, the valves of sand-adding device were shut off. During the IFTP stage, the valve of container C1 was shut off, and the valves of container C2 and tank 1 were opened. The smaller size TPA from tank 1 was mixed with the slickwater and then they would be pumped into the HF created during CF. After that, the ISTP fracturing was performed by closing abovementioned valves and opening the valves of container C3 and tank 2. Larger size TPA in tank 2 was used to plug the entrances of preferential HFs created during the CF and IFTP stages. In each stage, the pump was shut off until the designed fluid volume was injected.

(3) **Monitor and HF morphology analysis.** The wellhead pressure and AE events were recorded during the whole process. The fluctuate change of pressure and the generation of AE events may indicate the HF initiation, propagation, and diversion at different times. After the experiment, the trajectories of HFs created from the corresponding stage were identified according to colors of the fluorescent agent on the fracture surfaces. CT scanning was performed again to discover the HFs, the activated BPs, and NFs, and even the TPA distributions within each specimen. Based on the internal and external fractures observed, 3D fracture morphology can be reconstructed. Comprehensive analysis of the results of pressure curve, AE localization, and CT scan can accurately understand the timing of multi-HF generation in a horizontal well.

Fig. 4. (**a**) TPA of different particle sizes; (**b**) Static suspension of TPA in the slickwater.

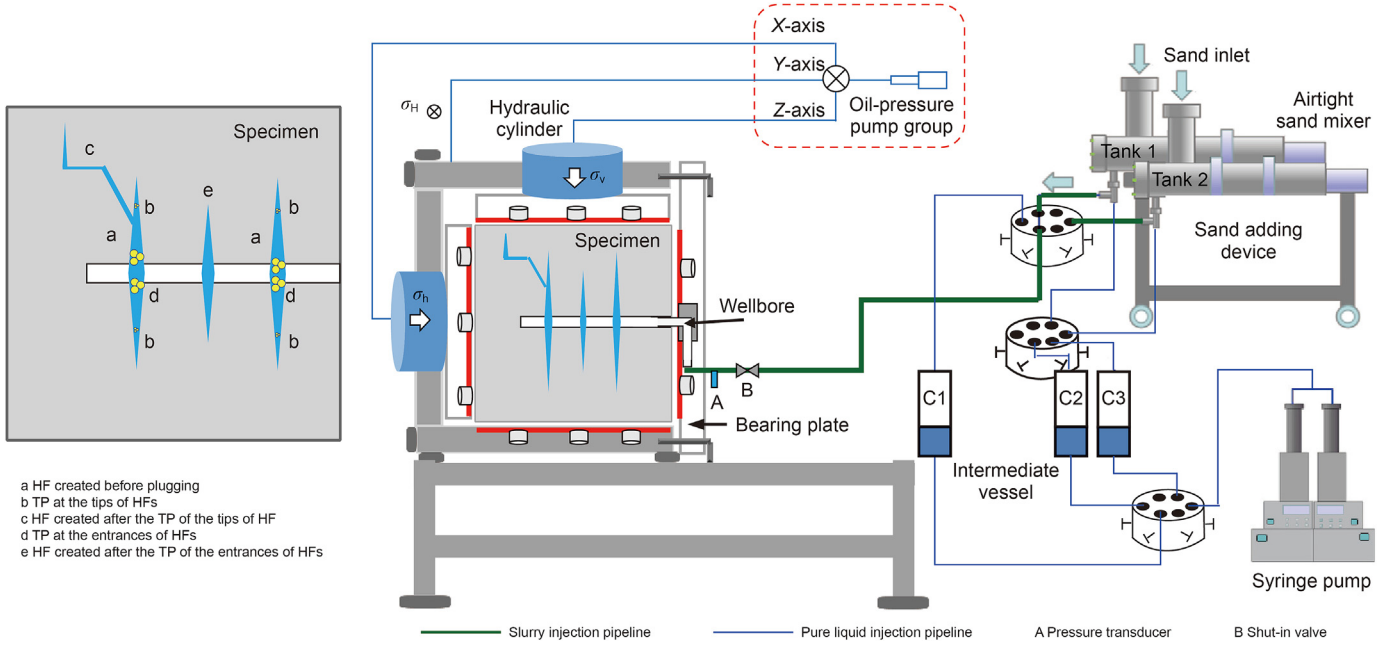

Fig. 5. Schematic diagram of the experimental instrument for TPDF simulation (modified from Zou et al., 2022).

3. Experimental results and analysis

3.1. Morphology of HFs and distribution of TPA

3.1.1. Fracturing with short stage spacing and few clusters per stage

Fig. 6 shows the HF morphology created in specimen 0# through fracturing with three stages and two clusters per stage. As shown in Fig. 6(c), in the middle and upper parts of specimen 0#, approximately two transverse hydraulic fracture (THFs, HF growth across the wellbore) were initiated from the two clusters in both the stages 1 and 3, while only one THF was initiated in the stage 2. These THFs nearly penetrated through the three opened BPs in the upper part of specimen 0#. In the lower part of specimen 0#, three THFs were initiated in the stage 1 and only one THF was initiated in

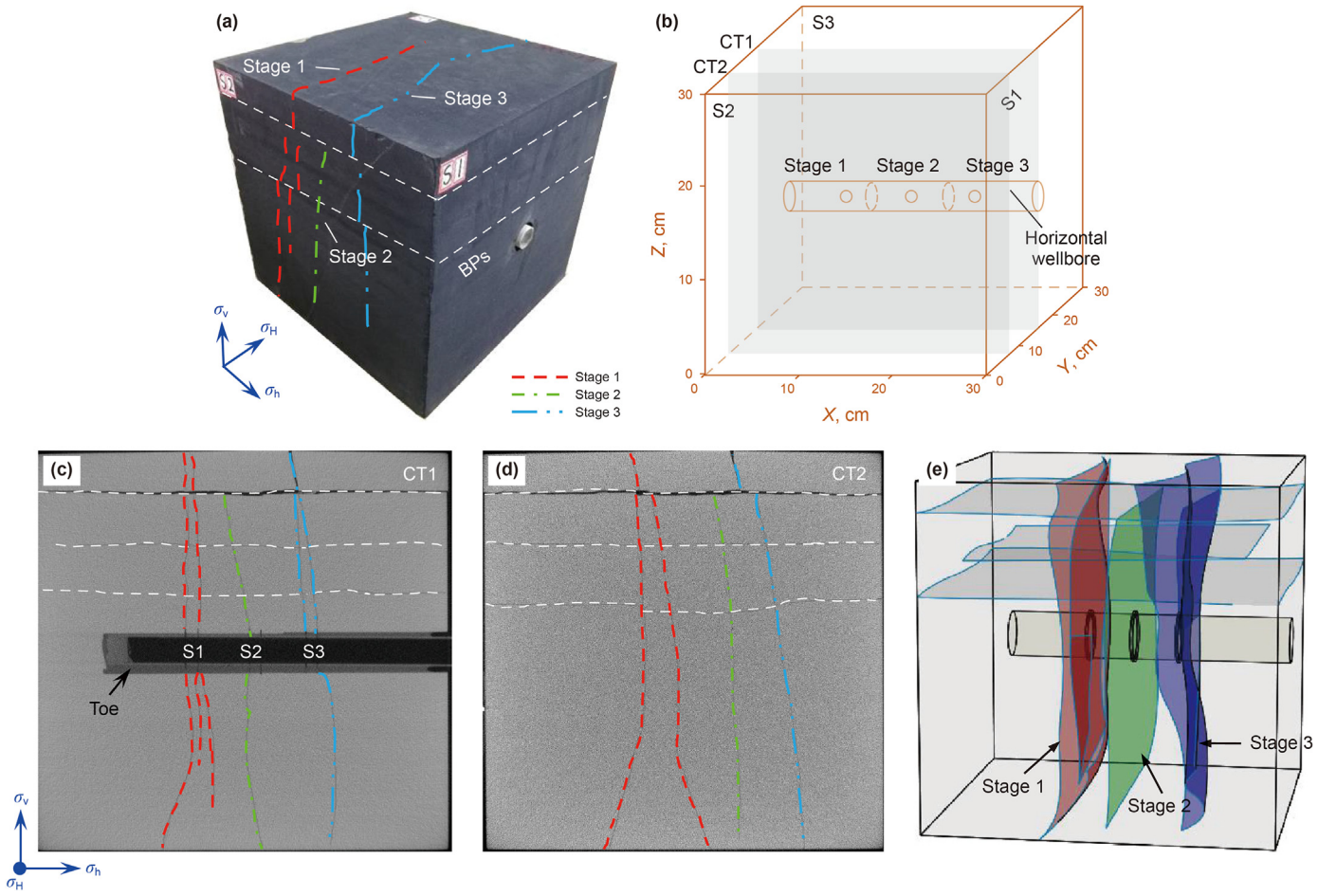

Fig. 6. HF morphology created in specimen 0# by multi-stage and multi-cluster fracturing in a horizontal well. (**a**) 3D view of physical image; (**b**) CT scanning position indicators; (**c**) Internal fracture morphology on CT1 ($Y = 15$ cm) along the wellbore; (**d**) Internal fracture morphology on CT2 ($Y = 5$ cm) parallel to the wellbore; (**e**) 3D reconstructed fractures.

the stages 2 and 3. As shown in Fig. 6(d), during the propagation process, fracture mergence and pinching-out, resulting from the interference among multi-fracture, may cause the reduction in the number of THFs as they propagate far from the wellbore. When the THFs encounter with the BPs, offset, diversion and/or termination may occur, which causes the local nonplanarity in the height direction. As a whole, the result indicates that the mode of "short stage spacing with few clusters" is conducive to uniform initiation and propagation of multi-fracture in a horizontal well, but in fact, it is inefficient and less economical in the field operation.

3.1.2. *Fracturing with long stage spacing and multiple clusters per stage*

Fig. 7 shows the fracture morphologies created in some representative specimens after TPDF. According to the occurrence of HF created in the specimens, three representative fracture patterns can be summarized, namely THF, longitude HF (LHF) (HF growth along the wellbore), and horizontal HF (HHF) (HF growth along the BP). It has been observed THFs were created in all the specimens (1#–20#), except for specimen 18#. HF morphologies are obviously affected by the BPs and NFs. Complex branches can form when HFs encounter with the NFs locally. HFs may be cut off or penetrate the BPs, and part of them may deflect from their original growth paths. As can be seen, compared with the fracturing mode of "short spacing stage with few clusters", the results of "long spacing stage and multi-cluster" mainly used in this study have greater uncertainty, and it is more necessary to clarify the matching of cluster number, TPA particle size combination and concentration to promote the uniform initiation and propagation of multi-fracture.

The transport of TPA inside the wellbore and the HFs can be preliminarily understood by observing the specimen surfaces and the fracture surfaces after the experiments. The TPA can enter the HFs, transport along the fractures to the surfaces of specimens, and deposit as the fluid flows out, as shown in Fig. 8. TPA tends to accumulate nearby the activated perforation clusters inside the wellbore. Meanwhile, TPA was unevenly distributed inside the HFs and plugging zone can be clearly observed, as shown in Fig. 8(d). The distribution regime of TPA greatly affects the diversion of HFs. It is necessary to slice the specimens after TPDF to obtain more detailed results, and then further discuss the distribution characteristics of TPA.

3.2. *Analysis of influencing factors on fracture morphology*

Based on the fracture morphologies and pressure curves, the effects of the particle size, concertation of TPA, and the number of perforation clusters on initiation, propagation, and diversion of multiple HFs were analyzed.

3.2.1. *The influence of particle size of TPA*

Multi-particle sizes combined TPA is often applied to improve the plugging efficiency inside the HFs (Chen et al., 2019; Zou et al., 2020; Wang Y. et al., 2020; Zhang et al., 2019). Experiments were performed on specimens 6#–9# to analyze the influence of TPA of

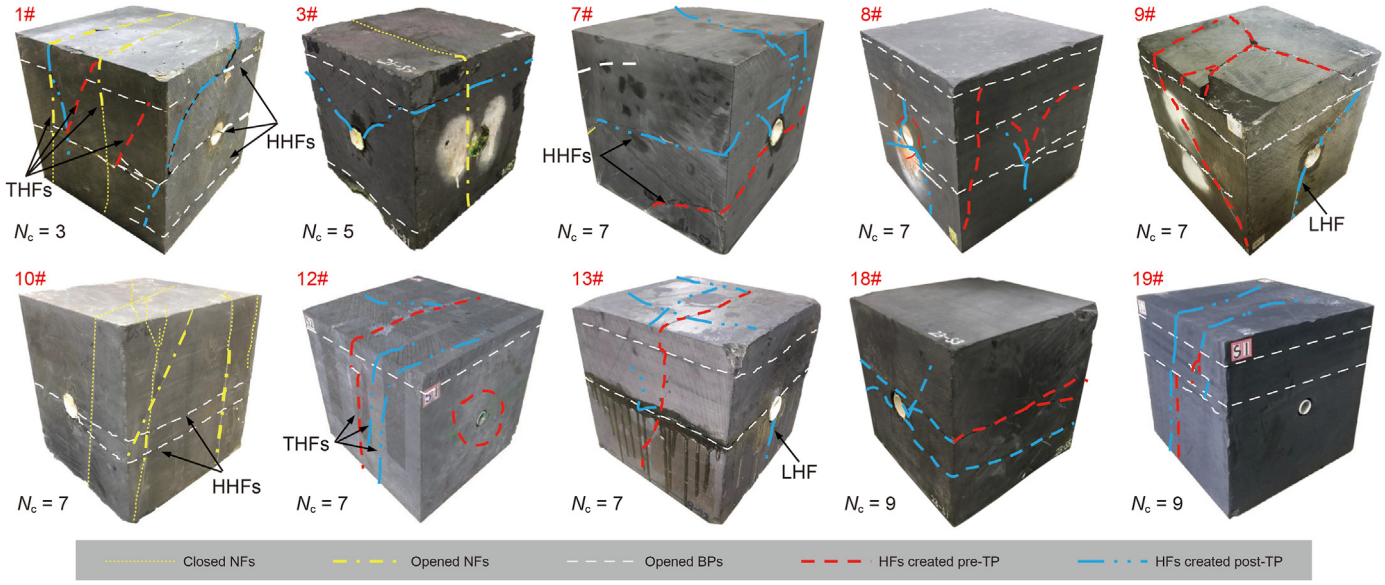

Fig. 7. HF morphologies created in several representative specimens after TPDF (N_c means the number of perforation clusters).

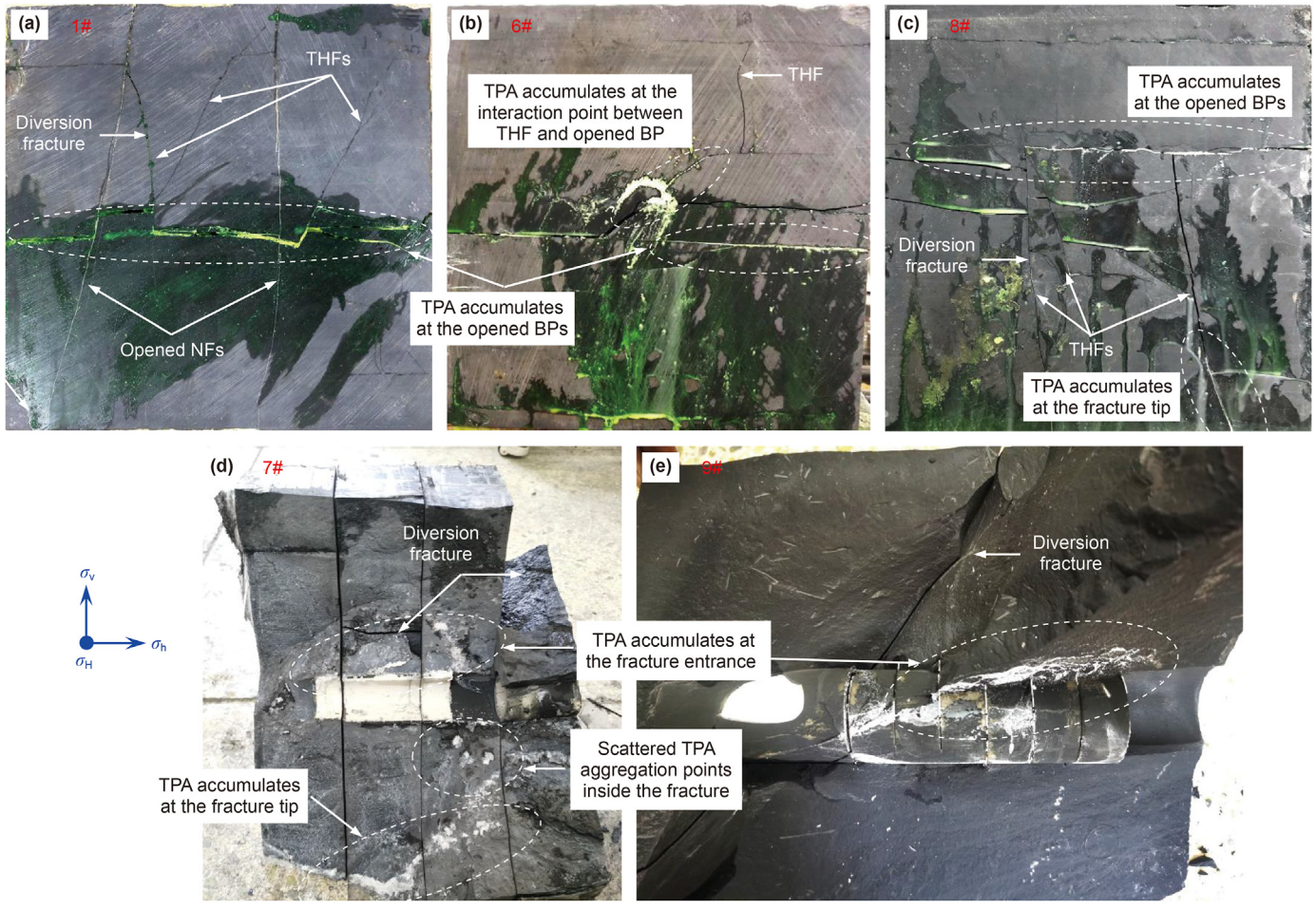

Fig. 8. Distribution of TPA on the surfaces and the interior of five representative specimens. (**a**) 6#; (**b**) 8#; (**c**) 1#; (**d**) 7 #; (**e**) 9#.

different particle size combinations on HF diversion. Figs. 9–11 show the peak pressures and HF morphologies created using different TPA particle size combinations. In this series of parameter sensitivity analysis, seven perforation clusters and TPA concentrations of 40 and 30 g/L during the IFTP and ISTP fracturing stages were used, respectively. At some point, the larger the particle size of

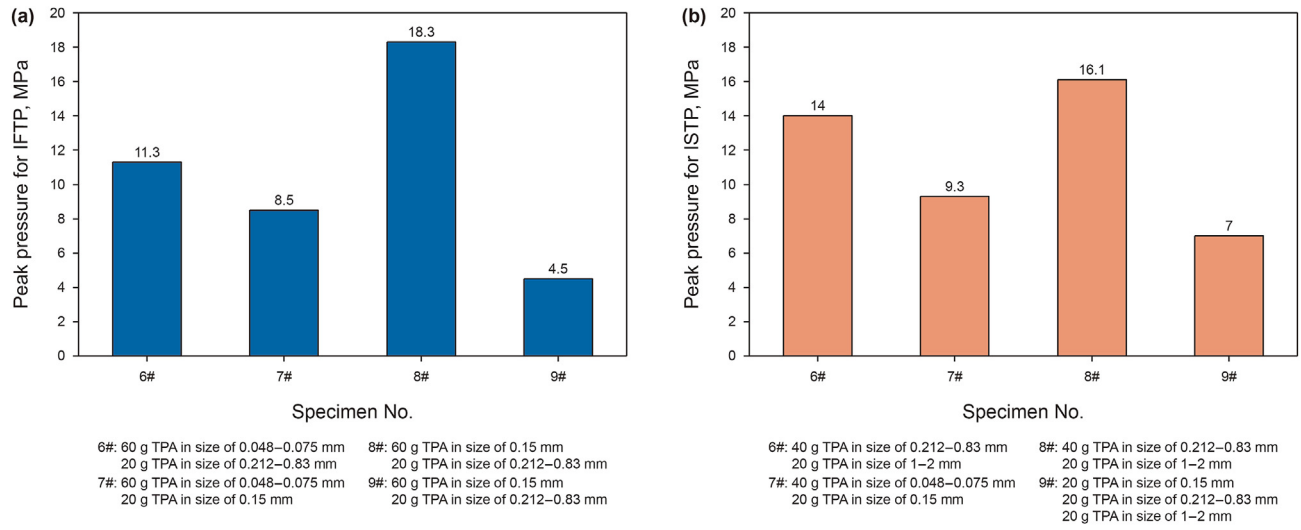

Fig. 9. Peak pressure for IFTP (**a**) and ISTP (**b**) using different TPA particle size combinations.

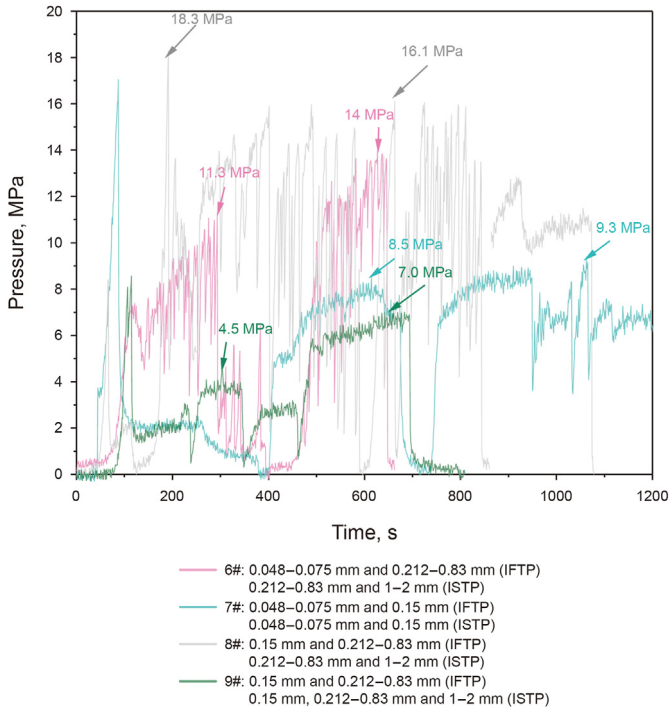

Fig. 10. Pressure curves of four specimens using different TPA particle size combinations.

TPA at the same concentration, the higher the peak pressures for the IFTP fracturing and ISTP fracturing are likely to be shown. Accordingly, more diversion fractures may be created, resulting in more complex in the overall fracture morphology in a specimen. In fact, the results are also largely dependent upon whether one or multiple THFs are already well-formed during CF. In both specimens 6# and 8#, two THFs are created during CF, and then multiple diversion fractures are created after temporary plugging. Higher peak pressures are present as a response, especially for the using larger TPA particle size combinations (60 g TPA in size of 0.15 mm and 20 g TPA in size of 0.212−0.83 mm during IFTP, and 40 g TPA in size of 0.212−0.83 mm and 20 g TPA in size of 1−2 mm during ISTP) in specimen 8#. Although the same TPA particle size combination as the specimen 8# are used in specimen 9# during IFTP fracturing, just a very low peak pressure (4.5 MPa) appears due to the absence of THF creation during CF. This observation also can be seen in specimen 7#.

In general, the preferential HFs created during the CF stage dominate the overall fracture complexity in each specimen; in the IFTP stage, almost no diversion fracture or branch was created from the preferential HFs, instead mainly to expand the preferential HFs and open the BPs around the horizontal wellbore; in the ISTP stage, the addition of large-size TPA can effectively build up higher pressure (Figs. 9 and 10), mainly to stimulate the uninitiated or under-initiated clusters and form new HFs. When HFs can propagate through the weakly opened BPs during the CF stage, multiple THFs may be created during the IFTP or/and ISTP fracturing stage, which is conducive to the generation of evenly distributed HFs in a specimen. This result can be seen clearly in the specimens 6# and 8#. On the contrary, when the BPs existing around the wellbore are opened widely during the CF stage, it is difficult to create THF during the IFTP or/and ISTP fracturing stage. In such case, the fracture height is likely limited, resulting in a relatively simple fracture morphology, as the result shown in specimen 7#.

3.2.2. The influence of TPA concentration and perforation cluster number

Fifteen specimens were used to analyze the influence of concentration of TPA and the number of perforation clusters on HF diversion and pressurization. Fig. 12 shows several representative HF morphologies created at different TPA concentration combinations and cluster numbers. Essentially, the higher the cluster number and the concentration of TPA are, the higher the number of diversion fractures formed and the higher the complexity of fracture morphology will be. However, it is worth mentioning that the activation of BPs nearby the wellbore may cause the poor plugging and diverting effect, and consequently the uncertainty in entire fracture morphology during the TPDF (e.g., for specimens 3#, 5#, 7#, and 16#), as shown in previous section. Among the specimens, specimen 11#, exhibiting the best plugging and diverting effect, wherein various types of fractures, including five THFs, one LHF (created during TPDF) and two HHFs were created using cluster number $N_c = 7$, and TPA concentration of 60 g/L for IFTP and 30 g/L for ISTP. Meanwhile, the peak pressure increases generally with the increase in TPA concentration under different cluster numbers, as

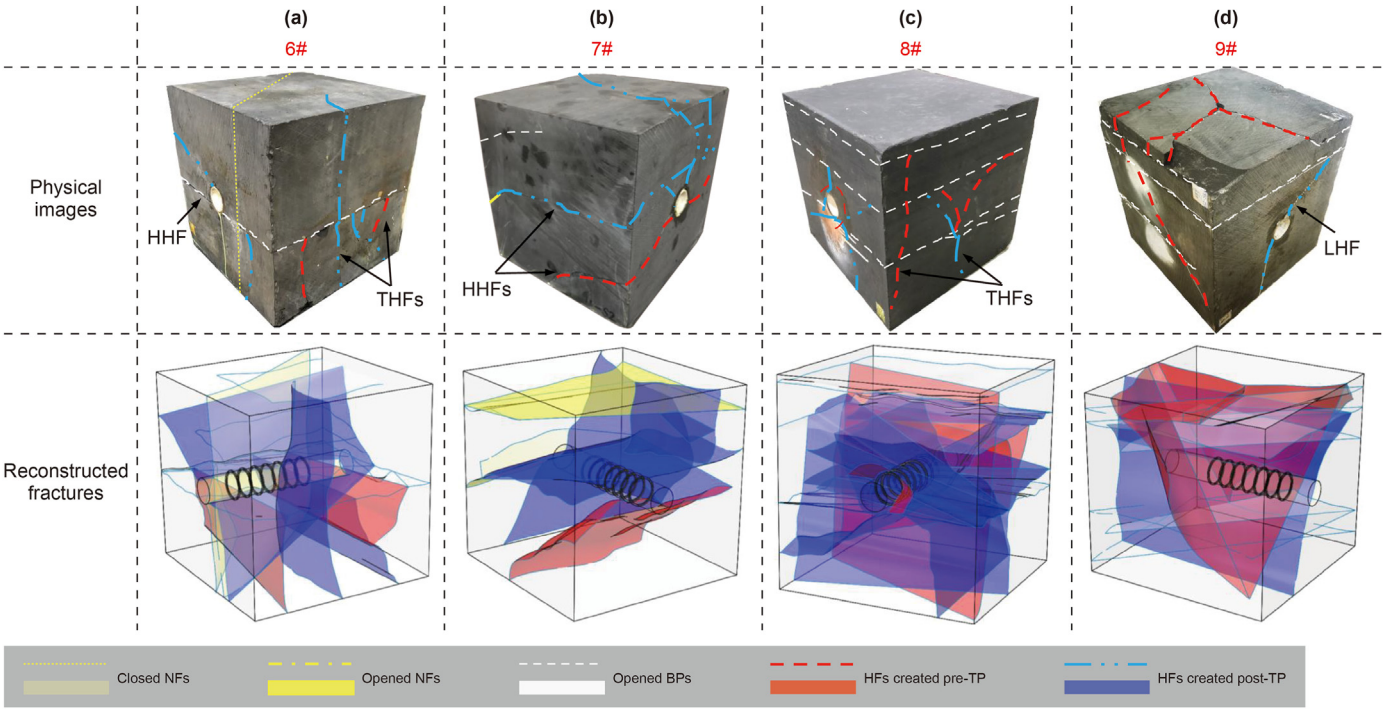

Fig. 11. HF morphologies created using different TPA size combinations for specimens. (**a**) 6#: 0.048–0.075 mm and 0.212–0.83 mm during IFTP, and 0.212–0.83 mm and 1–2 mm during ISTP; (**b**) 7#: 0.048–0.075 mm and 0.15 mm during IFTP, and 0.048–0.075 mm and 0.15 mm during ISTP; (**c**) 8#: 0.15 mm and 0.212–0.83 mm during IFTP, and 0.212–0.83 mm and 1–2 mm during ISTP; (**d**) 9#: 0.15 mm and 0.212–0.83 mm during IFTP, and 0.15 mm, 0.212–0.83 mm and 1–2 mm during ISTP.

shown in Fig. 13. Specifically, the less the cluster number (e.g., $N_c = 3$) the faster the peak pressure raises, and the more the cluster number (e.g., $N_c = 9$) the slower the peak pressure raises. In some specimens (e.g., 4#, 9#, 10#, 14#, 16#, and 18#), it was not easy to raise the peak pressure when the opened BPs or/and LHF created near the wellbore dominated the overall fracture growth pattern. With the same TPA size and amount, it appears that fewer clusters are more likely to display high peak pressure than more clusters during TPDF.

4. Discussion

4.1. Relationship among HF number, overall morphological complexity and pressure curve type

Three general types of pressure curves can be classified based on the overall fracture morphology and pressure curve characteristics (pressure value and fluctuation) observed in the twenty TPDF experiments conducted (Table 3). The pressure curves of specimens 1#, 6#, 8#, 11#, 12#, 19#, and 20# can be classified as type I (e.g., Fig. 14(a) and (b)), which exhibits a relatively high breakdown pressure (7.3–13.7 MPa, avg. 10.3 MPa) during CF, and it fluctuates violently and is moderately higher than the breakdown pressure during IFTP and ISTP. The peak pressures observed range from 11.3 to 18.4 MPa (avg. 15.3 MPa) during IFTP and 11.5–16.1 MPa (avg. 13.6 MPa) during ISTP, respectively. Compared to the breakdown pressure, the average increase in peak pressures is approximately 5 MPa for IFTP and 3.4 MPa for ISTP. In such case, multiple THFs or/and branches can be newly created during TPDF, indicating a good fracture diversion effect.

Compared to type I, pressure curve type II exhibits that the pressure fluctuates infrequently but maintains a high value during TPDF. Take specimens 3# and 15# for example, the peak pressures are far higher than the breakdown pressure (Fig. 14(c) and (d)). The peak pressures observed range from 11.2 to 18.7 MPa (avg. 15 MPa) during IFTP and 23.9–27.9 MPa (avg. 25.9 MPa) during ISTP, respectively. Compared to the breakdown pressure (8.2–13.1 MPa, avg. 10.7 MPa), the average increase in peak pressures is approximately 4.3 MPa for IFTP and 15.3 MPa for ISTP. Under this characteristic, a fair fracture diversion effect is observed, as evidenced by the creation of LHF along the wellbore or/and HHFs along slightly opened BPs, which subsequently activate the NFs during TPDF. Bad diversion effect appeared widely during TPDF, e.g. in specimens 4#, 9#, 10#, 14#, 16#, and 18#, which display the type III of pressure curve characteristics. In those specimens, the breakdown pressure (4.3–11.1 MPa, avg. 8 MPa) during CF is obviously lower than that of the specimens with the pressure curve type I or II. Moreover, the peak pressure was raised hardly beyond the breakdown pressures during TPDF. HFs mainly initiate along the largely opened BPs near wellbore, which may dominate the overall fracture morphology.

As shown in Fig. 15(a), an evident increasing trend in the number of new diversion fractures is observed with the escalation of peak pressures during IFTP and ISTP. Additionally, a consistent relationship is observed between the breakdown pressure during CF and the peak pressures for IFTP and ISTP. Moreover, the breakdown pressure and peak pressures during TPDF are generally higher when initiating THFs during the CF stage. Conversely, opening BPs near the wellbore leads to lower breakdown pressure, consequently resulting in a lower peak pressure during TPDF, as shown in Fig. 15(b). In such cases, the fracture morphology is predominantly influenced by the BPs near the wellbore, making it challenging to effectively plug the fracture and increase the pressure. The number of diversion fractures formed after TPDF shows a positive correlation with the peak pressure of TPDF. The formation of standard THFs during the CF stage proves advantageous for facilitating the formation of new fractures in TPDF. Conversely, the

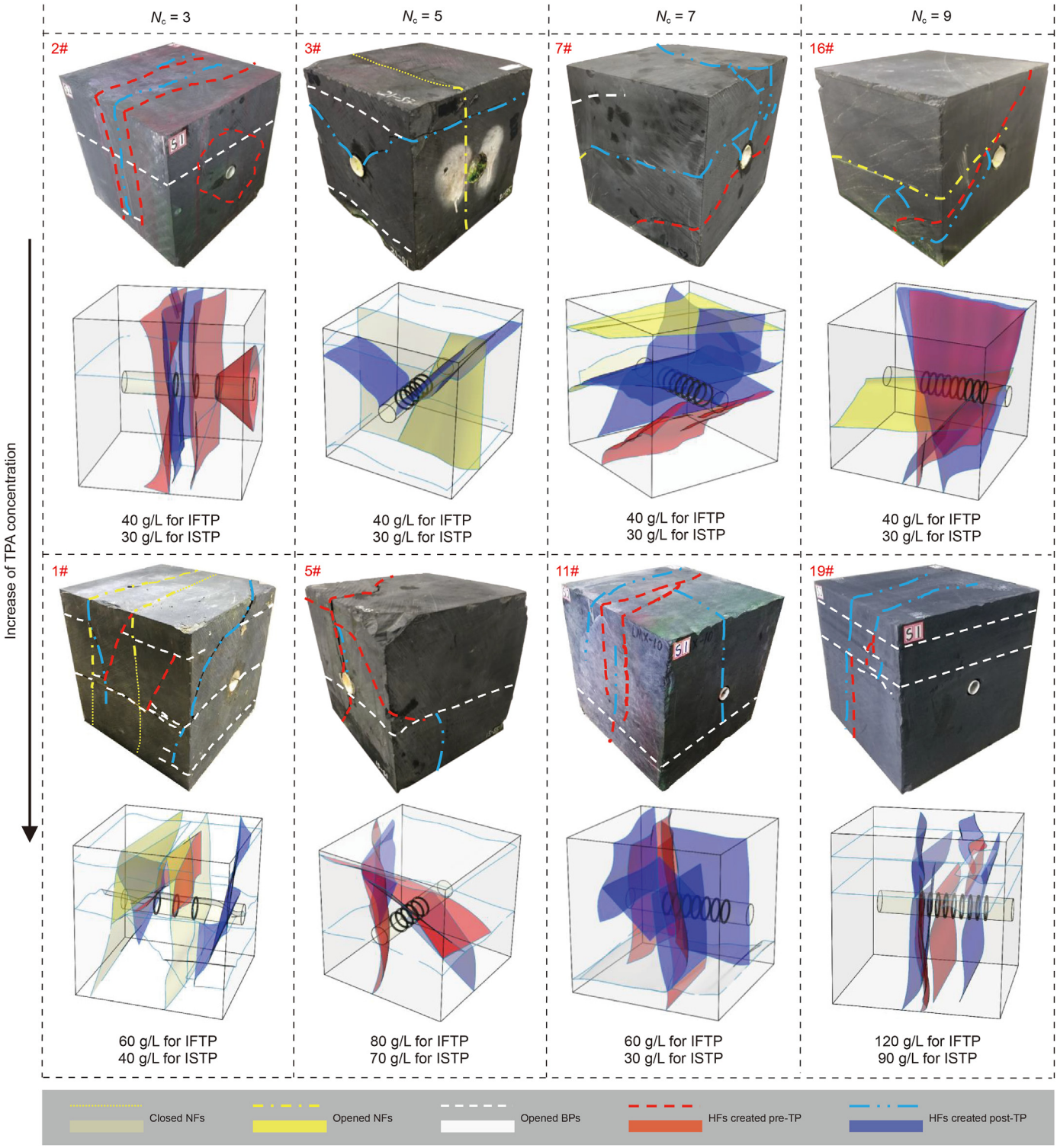

Fig. 12. Several representative HF morphologies created by using different TPA concentrations and cluster numbers (N_c).

presence of BPs connected to the wellbore hampers temporary plugging and limits pressure increase, consequently leading to poor diversion effects. Therefore, the choice of TPA concentration and/or particle size should be adjusted and optimized based on the pressure response during TPDF. In the latter scenario, a higher concentration and/or larger particle size may be more suitable.

4.2. Specimen slice-cutting analysis

To provide a more accurate depiction of the TPA distribution and fracture paths, six representative fractured specimens were sectioned after the experiments. Based on the observed fracture trajectories on the specimen surfaces, specimens 1#, 4#, and 12# were sliced parallel to the wellbore, while specimens 7#, 15#, and

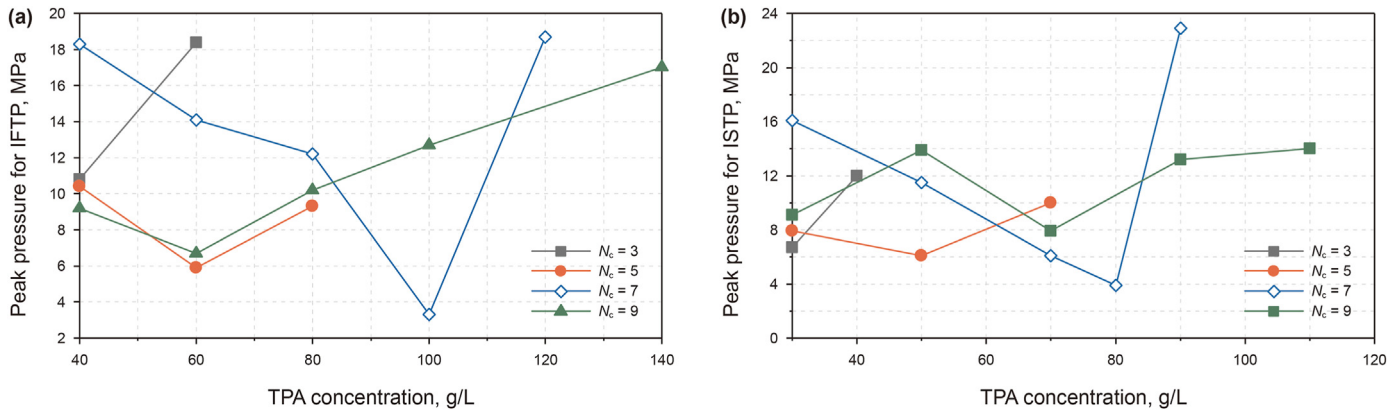

Fig. 13. Curves of peak pressure vs. TPA concentration for different cluster numbers (N_c) during IFTP fracturing (**a**) and ISTP fracturing (**b**).

Table 3
Diversion effects of three representative pressure curve types during the TPDF.

Pressure curve type	Curve features	Breakdown Pressure, MPa	Pressure for IFTP, MPa		Pressure for ISTP, MPa		Diversion effect	Typical specimen No.
			Peak value	Increment	Peak value	Increment		
I	Pressure fluctuates violently during TPDF and is moderately higher than the breakdown pressure	7.3–13.7/10.3	11.3–18.4/15.3	0.4–9.9/5.0	11.5–16.1/13.6	−2.2–7.7/3.4	Good: multiple THFs or/and branches can be newly created during TPDF	1#, 6#, 8#, 11#, 12#, 19#, and 20#
II	Pressure is relatively stable during TPDF, but far higher than the breakdown pressure	8.2–13.1/10.7	11.2–18.7/15.0	−1.9–10.5/4.3	23.9–27.9/25.9	14.8–15.7/15.3	Fair: LHF or/and HHFs growth along the slightly opened BPs and then activation the NFs	3# and 15#
III	Breakdown pressure is relatively low, but higher than the pressure during TPDF	4.3–11.1/8.0	4.5–10.2/7.0	−4.1–4.3/−1.1	3.9–9.3/7.1	−3.2–4.2/−0.9	Bad: HHF growth along the largely opened BP and then connection with the NFs	4#, 9#, 10#, 14#, 16#, and 18#

18# were sliced perpendicular to the wellbore (Fig. 16). The overall fracturing effect of the experiment was found to be satisfactory. Under the idealized laboratory conditions and with a well-executed cementing process, four out of the five perforation clusters were successfully opened (specimen 4#), resulting in an impressive 80% opening rate for the perforation clusters in some samples (Fig. 16(b)). Furthermore, Fig. 16(e) illustrates the formation of a complex fracture network through the penetration and opening of BPs. However, it should be noted that the penetration of fracture branches into the BP proved to be more challenging.

The locations where plugging occurs exhibit a wide range of diversity, which consequently affects the propagation of fractures in different ways. Firstly, the appearance of plugging effectively halts the propagation of the preferential fracture. The impermeable zone formed by TPA acts as a barrier, redirecting the fracture slightly and ultimately causing it to stop after merging with adjacent fractures, as shown in Fig. 16(a). When plugging happens at the tip of the fracture, as shown in Fig. 16(c) and (e), it initially expands the width of the primary fracture. If there are weak planes in close proximity to the fracture, it is easy to divert and initiate the weak planes, such as diverting and initiating the NF (Fig. 16(e)). However, if there are no weak planes nearby, diversion becomes still difficult, resulting in further expansion of the primary fracture width (Fig. 16(c)). Consequently, the impermeable zone faces a higher impact from the fluid due to the increased fracture width, leading to a shorter length of the impermeable zone and a higher degree of compaction caused by TPA accumulation. When plugging occurs in the middle of the fracture, as shown in Fig. 16(b), the impermeable zone becomes longer, and weak planes (BPs) are present near the plugging position. This leads to diversions occurring at this location and the opening of multiple BPs. On the other hand, when plugging occurs at the entrance of the fracture, an increase in circumferential stress around the well causes the fracture to initiate on the opposite side of the plugging position.

In addition, as shown in Fig. 16(a) and (b), the opened BP exhibits a tendency to expand more towards the surface of the specimen rather than towards the center. This behavior can be attributed to the fact that under triaxial stress conditions, the equivalent stress at any point within the specimen is higher than that at the surfaces. As one grows closer to the specimen surface, the equivalent stress decreases. Furthermore, Fig. 16(f) illustrates the observation of TPA accumulation in the wellbore, making it challenging for the buildup to enter the fracture. This accumulation phenomenon can be attributed to the high concentration of TPA present. Additionally, the fractures have a tendency to initiate at the bottom of the wellbore due to poor cementing quality. These fractures then propagate along the outer wall of the wellbore, penetrating the entire specimen. Radial fractures are also prone to forming at the wellhead and bottom of the wellbore, as shown in Fig. 16(c).

4.3. HFs diversion mechanism under the strike-slip fault stress state

Based on the analysis of the seismic source mechanism and CT scanning, we can accurately determine the temporal sequences and locations of HF generation. Fig. 17 shows the overlay images of AE event distribution and CT scanning across the wellbore of three representative specimens (e.g., specimens 8#, 12#, and 13#). In general, under the strike-slip fault stress state of the Longmaxi Formation, i.e., $\sigma_h = 10$ MPa, $\sigma_H = 25$ MPa, and $\sigma_V = 20$ MPa in the

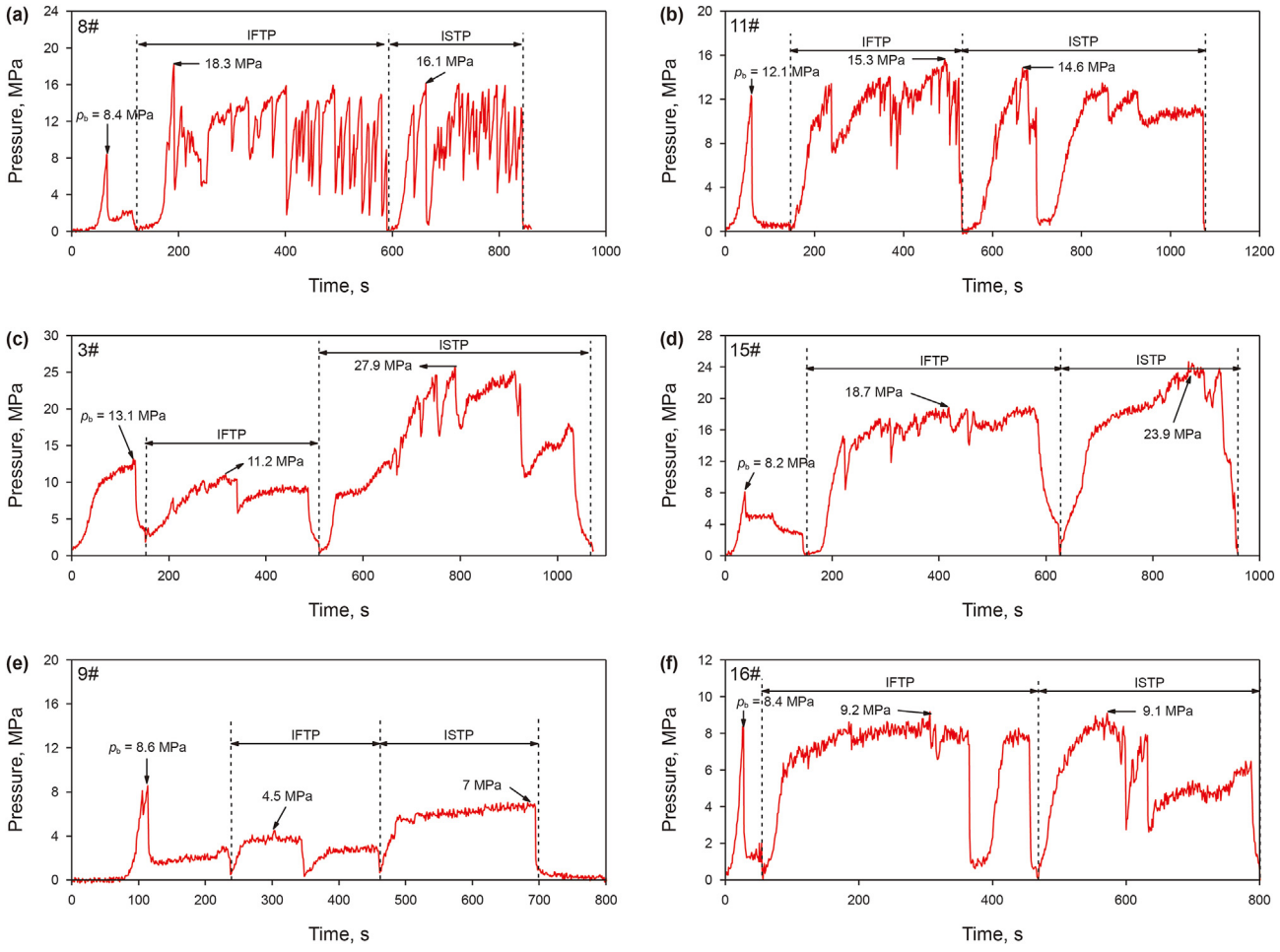

Fig. 14. Pressure curves of six representative specimens. (**a**) 8#; (**b**) 11#; (**c**) 3#; (**d**) 15#; (**e**) 9#; (**f**) 16#.

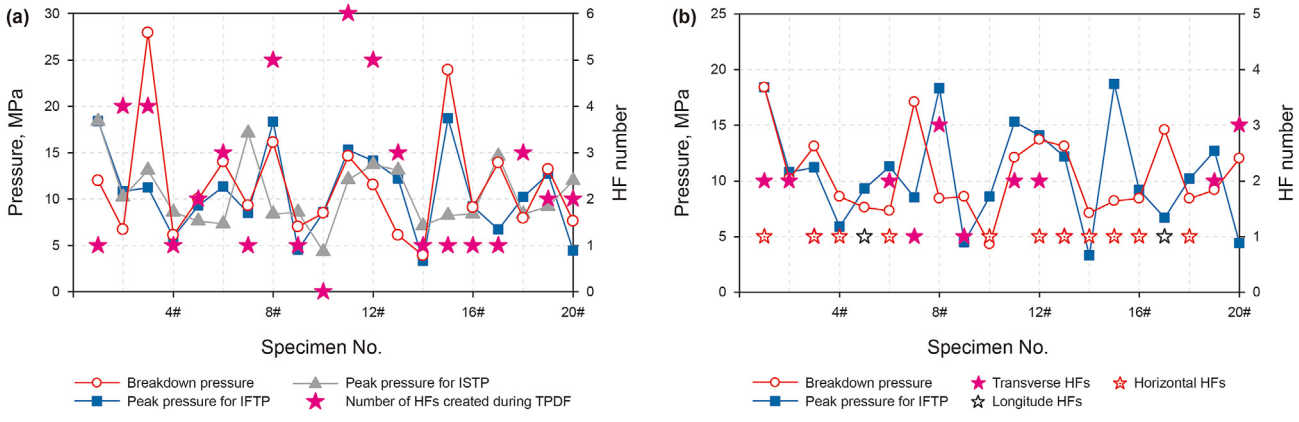

Fig. 15. (**a**) Relationship between fracture number and various pressures; (**b**) Relationship between fracture pattern and various pressures.

experiments as well, achieving diversion of vertical fractures during IFTP fracturing is challenging. Instead, it is more inclined to open BPs near the wellbore, creating HHFs with high conductivity. Consequently, only a relatively small number of AE events are generated. During IFTP fracturing, specimens with dense natural fractures (NFs) may experience local activation of NFs, but this does not significantly affect the overall fracture complexity. In specimens without NFs, under-propagated clusters and BPs near the wellbore may extend over a wide area. Even with a significant increase in pressure, it only results in the continued propagation of HFs from the under-opened clusters. Thus, both IFTP and ISTP mainly initiate unopened or under-opened perforation clusters.

To specific, as in specimen 8#, a total of 349 AE events were generated throughout the entire fracturing process, effectively indicating the growth trajectories of HF during different stages of fracturing. During the CF stage, three THFs initiated from clusters 2,

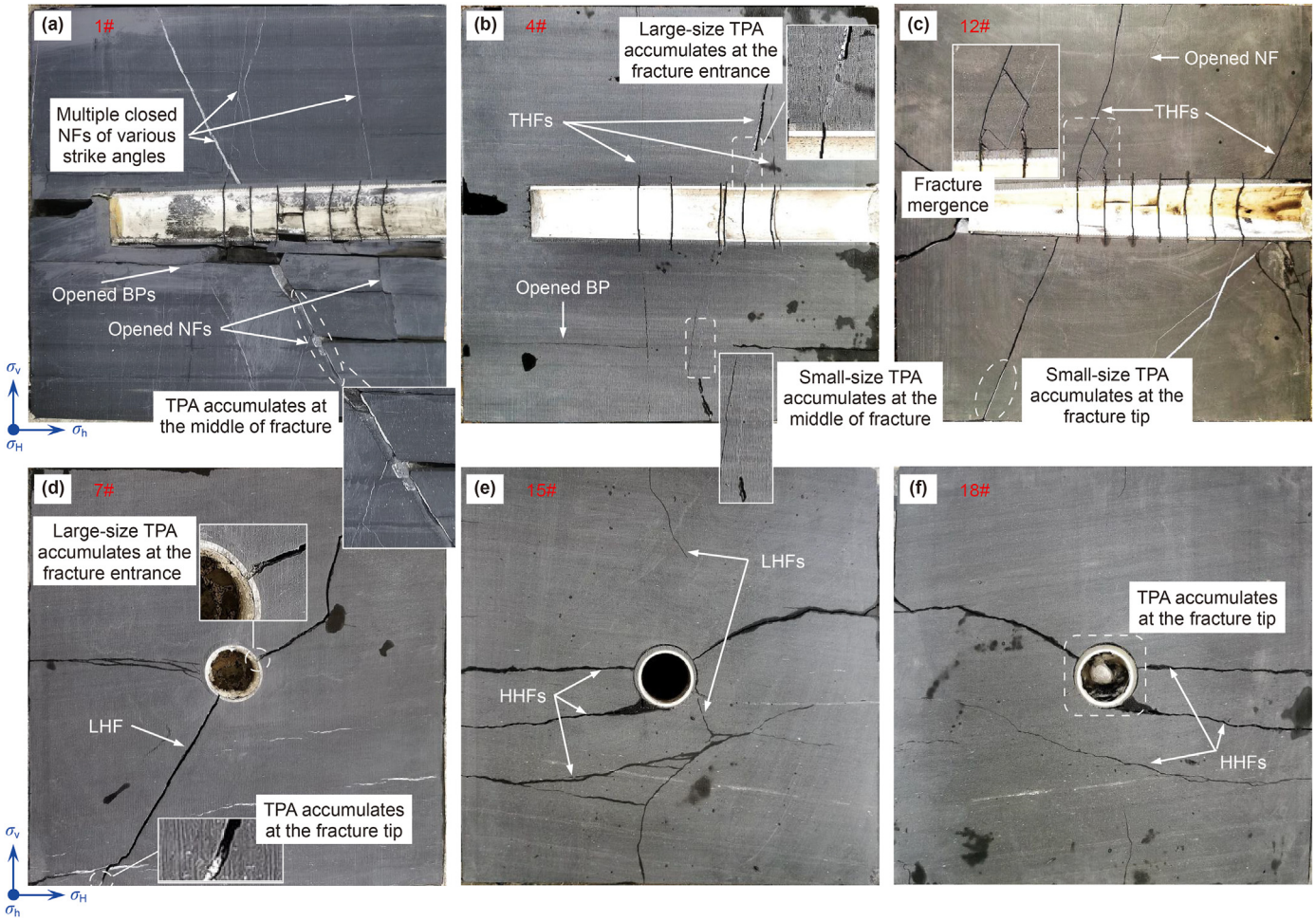

Fig. 16. Slice-cutting of six representative specimens. Specimens 1# (**a**), 4# (**b**), and 12# (**c**) sliced along the wellbore and 7# (**d**), 15# (**e**), and 18# (**f**) sliced perpendicular the wellbore.

6, and 7, and propagated asymmetrically. This is also evident in the distribution of AE events (represented by red dots), which numbered 111 and accounted for 31.8% of the total AE events. In contrast, during the IFTP fracturing, there was no creation of new fracture, as indicated by the limited number of AE events (represented by purple squares) near the wellbore. Only 25 AE events, representing 7.2% of the total, occurred during this stage. Subsequently, four clusters (C1, C3, C4, and C5) were newly opened during the ISTP fracturing. It is important to note that the growth of HFs (represented by blue lines) from clusters C3, C4, and C5 were cut off by the opened BPs located above and below the horizontal wellbore. However, the HF initiating from C1 propagated fully and was able to penetrate the entire specimen. A total of 213 AE events, accounting for 61% of the events, occurred during this period. Similar results were also observed in specimens 12# and 13#. The AE events generated during the IFTP fracturing were largely concentrated near the wellbore, indicating the opening of BPs in close proximity to the wellbore to create HHFs. More AE events were generated during the ISTP fracturing, illustrating that multiple HFs can initiate and propagate from unopened or partially under-opened perforation clusters.

4.4. Application examples

The first and second stages of Well-X are adjacent stages of the Xth horizontal well, with a vertical length of 3200 m and a horizontal length of 1540 m targeting the Longmaxi Formation. Multi-cluster hydraulic fracturing was carried out on each stage, with three pumping phases in each stage. The first phase was a water frac to create fractures, and TPA was added in the second and third phases to divert the fractures. The main difference between the two stages lies in the amount and size of the TPA used, as shown in Table 4. The experimental results on the particle size and dosage of the TPA are converted to field scale and applied to the fracturing construction of the second stage using similarity criteria. Eqs. (3) and (4) are similarity formulas for the particle size of the TPA used in two temporary plugging fracturing phases (i.e., the second and third pumping phases), which correspond to IFTP and ISTP in the experiments, respectively. Eqs. (5) and (6) represent similarity formulas for the dosage of the TPA. The values of symbols in equations are shown in Table 5. It should be noted that the dosage of the TPA (M_{1M} and M_{2M}) under laboratory conditions refers to the actual injection volume at the peak pressure. Additionally, considering factors such as settlement of the in-stage TPA in the wellbore, partial entry of the in-stage TPA into the fractures, and enlargement of perforation hole diameter due to erosion, there is a design safety factor γ ($\gamma = 0.5$) to account for the loss of the in-stage TPA used in third pumping phase.

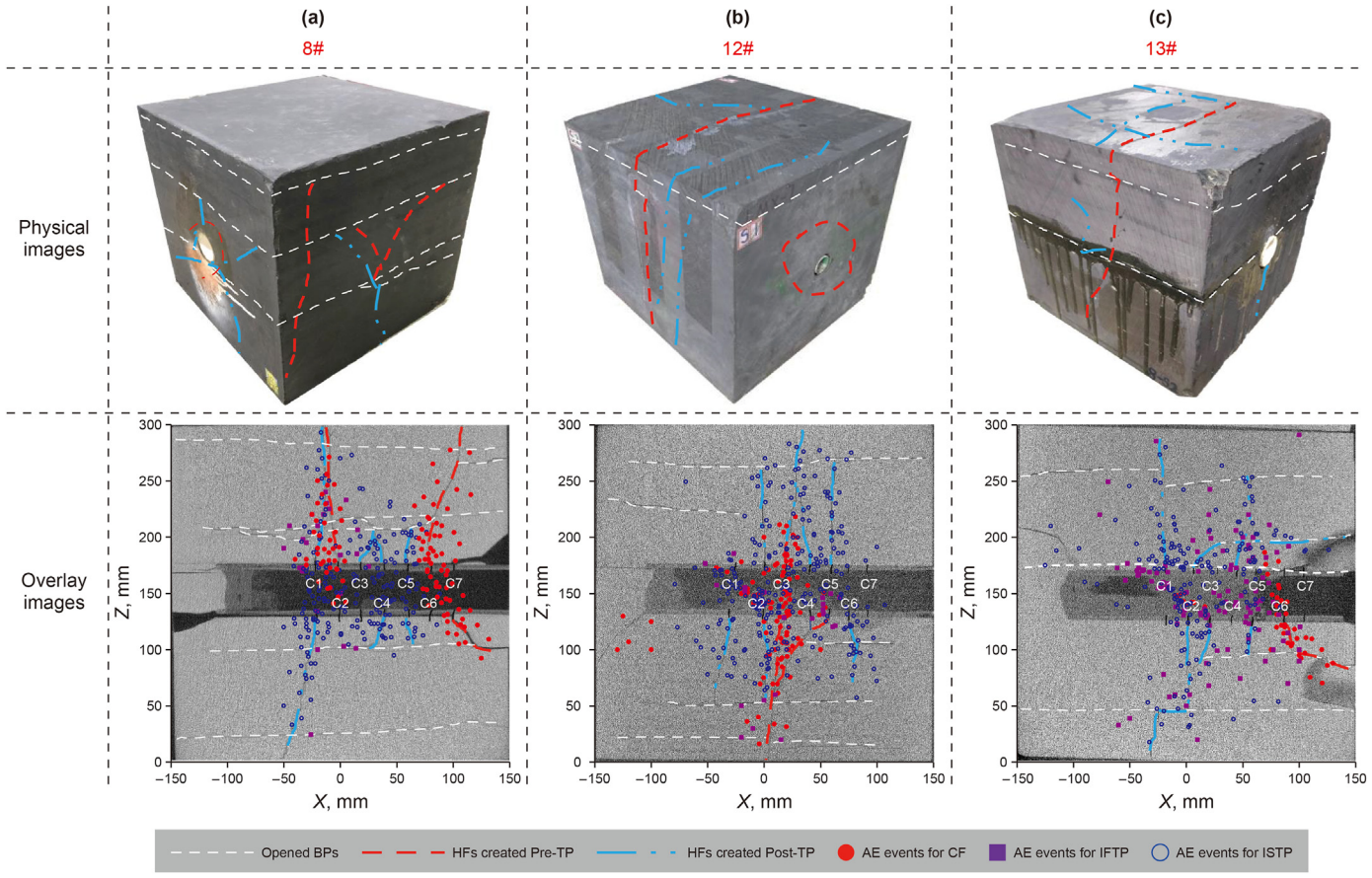

Fig. 17. Overlay images of AE event distribution and CT scanning across the wellbore of three representative specimens. (**a**) 8#; (**b**) 12#; (**c**) 13#.

Table 4
The temporary plugging agent parameter scheme for the first and second stages of Well-X.

Stage number of Well-X	Second pumping phase		Third pumping phase	
	Particle size, mm	Amount, kg	Particle size, mm	Amount, kg
First	0.212–0.83	30.0	1–2	30.0
Second	1.5	81.0	1, 3, 5	23.0, 13.8, 9.2 (total 46.0) [b]
	2, 4, 6	13.5, 8.1, 5.4 (total 27.0) [a]	6, 8, 10	11.5, 6.9, 4.6 (total 23.0) [c]

Notes: (a), (b), and (c): In different TPA particle size combinations, the TPA with three different particle sizes accounts for 50%, 30%, and 20%, respectively, its ratio is consistent with the experimental results of temporary plugging agent particle size ratio.

Table 5
Specific values of parameters used.

D_{1M}, mm	D_{2M}, mm	W_M, mm	W_F, mm	n_M	n_F	L'_M, cm	L'_F, cm	h_M, m	h_F, m
0.15 + 0.212–0.83	0.212–0.83 + 1–2	1	6–10	6	9	3	20–30	0.3	20–30
M_{1M}, g	M_{1M}, mm	d_n, mm	d_p, mm	l_n, mm	l_p, mm	w, mm	N	K	
13	10	22	15	3	1500	3	7	37	

$$\frac{D_{1M}}{D_{1F}} = \frac{W_M}{W_F} \tag{3}$$

$$\frac{D_{2M}}{D_{2F}} = \frac{w}{d_p} \tag{4}$$

$$\frac{M_{1M}}{M_{1F}} = \frac{n_M L'_M h_M W_M}{n_F L'_F h_F W_F} \tag{5}$$

$$\frac{M_{2M}}{M_{2F}} = \gamma \frac{N w d_n l_n}{K (d_p/2)^2 l_p} \tag{6}$$

where D is the particle size, mm; M is TPA dosage, g; n is the number of fractures; W is the fracture width, mm; h is the fracture

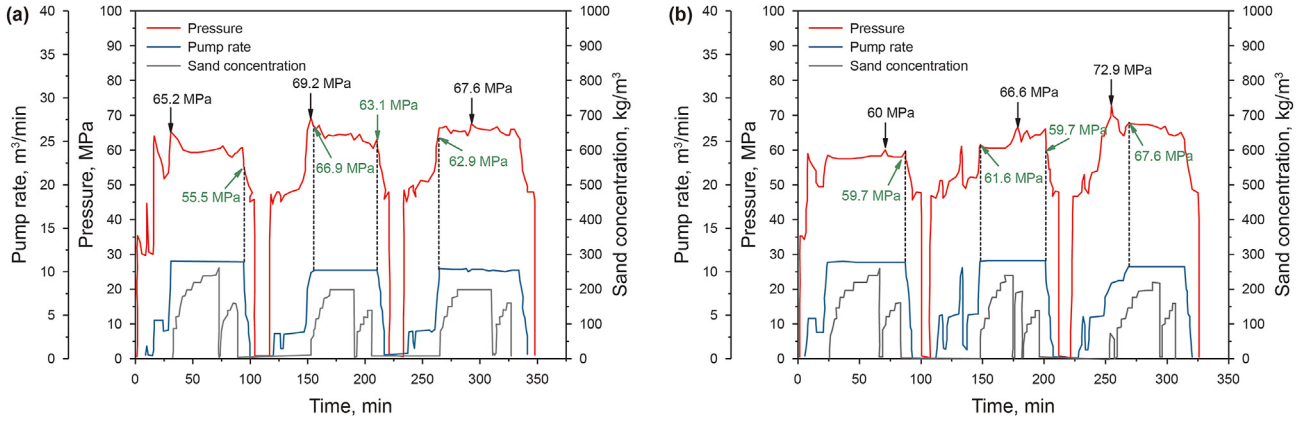

Fig. 18. The segmented fracturing construction curve of Well-X. (**a**) First stage; (**b**) Second stage.

height, m; d_n and d_p are the diameters of notch and perforation, respectively, mm; l_n and l_p are the lengths of notch and perforation, respectively, mm; w is the notch width, mm; K is the effective number of perforations; L' is the plugging length, cm; N is the number of clusters; subscripts 1 and 2 represent the first and second temporary plugging fracturing phases, respectively; subscripts M and F represent experimental parameters and field parameters, respectively.

According to the fracturing curve in Fig. 18, the injection pressure during the pre-fluid pumping phase in both stages was high, which resulted in a small increase in displacement and a rapid increase in pressure, indicating narrow and tortuous near-well fractures. After the first reduction in displacement, continuous sand addition was initiated. As the displacement stabilized, the pressure gradually decreased, indicating the need to add TPA in subsequent fracturing operations. In the second pumping phase of the first stage, a small particle size TPA (0.212–0.83 mm) was added at the amount of 30 kg when the displacement was reduced to 1 m^3/min, as shown in Fig. 18(a). The pressure reached a peak of 69.2 MPa after the displacement stabilized, which was 4 MPa higher than the first pumping phase. The pressure fluctuated slightly thereafter. In the third pumping phase, a larger particle size TPA (1–2 mm) was added at the amount of 30 kg when the displacement was reduced to 1 m^3/min. The pressure did not increase significantly compared to the second phase and showed no significant fluctuations. The pressure reached 66.9 MPa when the pump was stopped for the first time, which was 11.4 MPa higher than before, indicating a good effect from the first phase. The pressure reached 62.9 MPa when the pump was stopped for the second time, which was 0.2 MPa lower than before, indicating a poor temporary plugging effect. Overall, the first stage of Well-X achieved some results with a single particle size TPA according to the predetermined plan, but the effect was not significant.

As shown in Fig. 18(b), the experimental results were used to guide the fracturing of the second stage of Well-X, which used a combination of particle sizes of TPA shown in Table 4, and the amount of TPA was adjusted in a timely manner based on the pressure fluctuations. In the second pumping phase, considering the narrow and tortuous near-well fractures, a smaller particle size TPA combination (81 kg of 1.5 mm TPA and 27 kg of 2–6 mm TPA) was added. After the displacement stabilized, the pressure fluctuated significantly, reaching a peak pressure of 66.6 MPa, which was 6.6 MPa higher than the first pumping phase, indicating a significant temporary plugging effect. The pressure curve of the second phase reflected high temporary plugging back pressure and frequent pressure fluctuations, indicating the generation of complex fractures with wider apertures. Therefore, in the third pumping phase, the amount of the TPA was dynamically increased, using 46 kg of 1–5 mm TPA and 23 kg of 6–10 mm TPA, which resulted in a pressure increase of 6.3 MPa. Overall, under the guidance of the experimental conclusions, both temporary plugging phase of the second stage of Well-X achieved significant effects. Field practice has proven the validity of the conclusions regarding the TPA parameters obtained from the experiments, and the pressure fluctuations and their intensity reflect the opening of the diverted fractures, which are an effective indicator for guiding temporary plugging hydraulic fracturing operations on field.

5. Conclusions

In this paper, a series of laboratory TPDF experiment with multiple clusters in horizontal well were performed on the shale of Longmaxi Formation. The following conclusions can be drawn.

(1) According to the peak pressure, the combination of 60 g TPA in size of 0.15 mm and 20 g in size of 0.212–0.83 mm is the best for IFTP, while the combination of 40 g TPA in size of 0.212–0.83 mm and 20 g in size of 1–2 mm is the best for ISTP.
(2) With the increase in TPA concentration and number of perforation clusters, there is a trend of increasing the number of transverse fractures and the overall complexity of fracture morphology, and the number of perforation clusters is positively correlated with the demanded TPA concentration.
(3) The creation of transverse HFs or/and complex fractures mainly corresponds to the peak value and continuous fluctuation phase of the pressure curve during TPDF. Compared with the breakdown pressure of conventional fracturing, the peak pressure during TPDF is increased by more than 5 MPa.
(4) The breakdown pressure has a consistent trend with the peak pressure during TPDF. The number of diversion fractures correlates positively with the peak pressure of TPDF. The formation of standard transverse HFs during CF facilitate the generation of new fractures during TPDF, while wellbore-connected BPs hinder pressure lifting, resulting in poor diversion effectiveness. Adjustments in TPA concentration are recommended based on the analysis of pressure characteristics, fracture initiation and propagation morphology during CF stage.
(5) Under the stress state of strike-slip faults, it is challenging to achieve fracture diversion during the IFTP fracturing stage.

Furthermore, in the stage of ISTP fracturing, there is a tendency for the initiation of unopened or under-opened perforation clusters.

(6) Under laboratory experimental conditions, larger TPA particles tend to accumulate at the wellbore's toe or bottom, and the fracturing fluid mixed with TPA enters fractures solely through near-heel perforation clusters, resulting in the transverse fractures which can penetrate the BPs mainly near the heel of the wellbore. In this scenario, there is an inverse relationship between the number of clusters and both peak pressure and BP penetration ability.

(7) The pressure fluctuations and their intensity are effective indicators for guiding temporary plugging hydraulic fracturing operations on field. In the context of hydraulic fracturing operations, it is essential to dynamically adjust the dosage and particle size of TPA based on the fluctuation patterns observed in the pressure curve.

CRediT authorship contribution statement

Yu-Shi Zou: Writing – review & editing, Investigation, Formal analysis, Data curation, Conceptualization. **Can Yang:** Writing – original draft, Formal analysis. **Shi-Cheng Zhang:** Methodology. **Xin-Fang Ma:** Resources. **Yan-Chao Li:** Conceptualization. **Long-Qing Zou:** Conceptualization.

Declaration of competing interest

The authors declare that they have no known competing financial interests or personal relationships that could have appeared to influence the work reported in this paper.

Acknowledgments

This paper was supported by the National Natural Science Foundation of China (Grant No. 51974332).

References

Ali, N.D., Kamran, G., Kaveh, A., Yan, J., 2016. Mechanism of fracture initiation and propagation using a tri-axial hydraulic fracturing test system in naturally fractured reservoirs. European Journal of Environmental and Civil Engineering 20 (5), 560–585. https://doi.org/10.1080/19648189.2015.1056384.

Ali, N.D., Kamran, G., Kaveh, A., Yan, J., Aram, B., 2017. 3D Numerical modeling of the propagation of hydraulic fracture at its intersection with natural (pre-existing) fracture. Rock Mech. Rock Eng. 50 (2), 367–386. https://doi.org/10.1007/s00603-016-1097-7.

Bai, Q.S., Liu, Z.H., Zhang, C.W., Fang, T., 2020. Geometry nature of hydraulic fracture propagation from oriented perforations and implications for directional hydraulic fracturing. Comput. Geotech. 125, 103682. https://doi.org/10.1016/j.compgeo.2020.103682.

Chen, M., Zhang, S.C., Zhou, T., Ma, X.F., 2020. Optimization of in-stage diversion to promote uniform planar multifracture propagation: a numerical study. SPE J. 25 (6), 3091–3110. https://doi.org/10.1007/s00603-016-1097-7.

Chen, X.Y., Zhao, J.Z., Li, Y.M., Yan, W.Y., Zhang, X., 2019. Numerical simulation of simultaneous hydraulic fracture growth within a rock layer: implications for stimulation of low-permeability reservoirs. JGR Solid Earth 124, 13227–13249. https://doi.org/10.1029/2019JB017942.

Daneshy, A., 2020. Mechanics of fracture propagation in closely spaced clusters. In: SPE Annual Technical Conference and Exhibition. https://doi.org/10.2118/201675-MS.

Dontsov, E.V., Suarez-Rivera, R., 2020. Propagation of multiple hydraulic fractures in different regimes. Int. J. Rock Mech. Min. Sci. 128, 104270. https://doi.org/10.1016/j.ijrmms.2020.104270.

Duan, K., Kwok, C., Zhang, Q., Shan, J.L., 2020. On the initiation, propagation and reorientation of simultaneously-induced multiple hydraulic fractures. Comput. Geotech. 117, 1–15. https://doi.org/10.1016/j.compgeo.2019.103226.

Guo, T.K., Tang, S.J., Liu, S., Liu, X.Q., Xu, J.C., Qi, N., Rui, Z.H., 2020. Physical simulation of hydraulic fracturing of large-sized tight sandstone outcrops. SPE J. 26, 372–393. https://doi.org/10.2118/204210-PA.

King, G.E., 2010. Thirty years of gas shale fracturing: what have we learned. In: SPE Annual Technical Conference and Exhibition. https://doi.org/10.2118/1110-0088-JPT.

Lecampion, B., Desroches, J., 2015. Simultaneous initiation and growth of multiple radial hydraulic fractures from a horizontal wellbore. J. Mech. Phys. Solid. 82, 235–258. https://doi.org/10.1016/j.jmps.2015.05.010.

Lei, B., Zuo, J.P., Coli, M., Yu, X., Li, Y., Liu, H.Y., 2024. Investigation on failure behavior and hydraulic fracturing mechanism of Longmaxi shale with different bedding properties. Comput. Geotech. 167, 106081. https://doi.org/10.1016/j.compgeo.2024.106081.

Li, M.H., Zhou, F.J., Sun, Z.H., Dong, E., Yuan, L.S., Wang, B., 2022. Experimental study on plugging performance and diverted fracture geometry during different temporary plugging and diverting fracturing in Jimusar Shale. J. Petrol. Sci. Eng. 215, 110580. https://doi.org/10.1016/j.petrol.2022.110580.

Li, N., Zhang, S.C., Ma, X.F., Zou, Y.S., Chen, M., Li, S.H., Zhang, Y.N., 2017. Experimental study on the propagation mechanism of hydraulic fracture in glutenite formations. Chin. J. Rock Mech. Eng. 36 (10), 2383–2392. https://doi.org/10.13722/j.cnki.jrme.2017.0159 (in Chinese).

Li, N., Zhang, S.C., Zou, Y.S., Ma, X.F., Wu, S., Zhang, Y.N., 2018a. Experimental analysis of hydraulic fracture growth and acoustic emission response in a layered formation. Rock Mech. Rock Eng. 51 (4), 1047–1062.l. https://doi.org/10.1007/s00603-017-1383-z.

Li, N., Zhang, S.C., Zou, Y.S., Ma, X.F., Zhang, Z.P., Li, S.H., Chen, M., Sun, Y.Y., 2018b. Acoustic emission response of laboratory hydraulic fracturing in layered shale. Rock Mech. Rock Eng. 51, 3395–3406. https://doi.org/10.1007/s00603-018-1547-5.

Liu, N.Z., Zhang, Z.P., Zou, Y.S., Ma, X.F., Zhang, Y.N., 2018. Propagation law of hydraulic fractures during multi-staged horizontal well fracturing in a tight reservoir. Petrol. Explor. Dev. 45 (6), 1059–1068. https://doi.org/10.1016/S1876-3804(18)30116-2 (in Chinese).

Lu, W., He, C., 2022. Numerical simulation on the initiation and propagation of synchronous perforating fractures in horizontal well clusters. Eng. Fract. Mech. 266, 108–412. https://doi.org/10.1016/j.engfracmech.2022.108412.

Ma, X.F., Li, N., Yin, C.B., Li, Y.C., Zhou, Y.S., Wu, S., He, F., Wang, X.Q., Zhou, T., 2017. Hydraulic fracture propagation geometry and acoustic emission interpretation: a case study of Silurian Longmaxi Formation shale in Sichuan Basin, SW China. Petrol. Explor. Dev. 44 (6), 1030–1037 (in Chinese).

Manchanda, R., Bryant, E.C., Bhardwaj, P., Philip, C., Mukul, M.S., 2018. Strategies for effective stimulation of multiple perforation clusters in horizontal wells. SPE Prod. Oper. 33, 539–556. https://doi.org/10.2118/179126-PA.

Olson, J.E., 2008. Multi-fracture propagation modeling: applications to hydraulic fracturing in shales and tight gas sands. The 42nd US Rock Mechanics Symposium (USRMS).

Qin, M.Q., Yang, D.S., Chen, W.Z., 2023. Numerical investigation of hydraulic fracturing in a heterogeneous rock mass based on peridynamic. Rock Mech. Rock Eng. 56, 4485–4505.

Salimzadeh, S., Usui, T., Paluszny, A., Zimmerman, R.W., 2017. Finite element simulations of interactions between multiple hydraulic fractures in a poroelastic rock. Int. J. Rock Mech. Min. Sci. 99, 9–20. https://doi.org/10.1016/j.ijrmms.2017.09.001.

Shi, S.Z., Cheng, F.S., Wang, M.X., Wang, J., Lv, W.J., Wang, B., 2022. Hydrofracture plugging mechanisms and evaluation methods during temporary plugging and diverting fracturing. Energy Sci. Eng. 10 (3), 790–799. https://doi.org/10.1002/ese3.1054.

Snyder, J., Cramer, D., White, M., 2021. Improved treatment distribution through oriented perforating. In: SPE Hydraulic Fracturing Technology Conference and Exhibition. https://doi.org/10.2118/204203-MS.

Tan, P., Chen, Z.W., Fu, S.H., Zhao, Q., 2023. Experimental investigation on fracture growth for integrated hydraulic fracturing in multiple gas bearing formations. Geoenergy Science and Engineering 231 (A), 212316. https://doi.org/10.1016/j.geoen.2023.212316.

Tang, X.H., Zhu, H.Y., Che, M.G., Wang, Y.H., 2023. Complex fracture propagation model and plugging timing optimization for temporary plugging fracturing in naturally fractured shale. Petrol. Explor. Dev. 50 (1), 139–151 (in Chinese).

Wang, B., Zhou, F.J., Yang, C., Wang, D.B., Yang, K., Liang, T.B., 2020. Experimental study on injection pressure response and fracture geometry during temporary plugging and diverting fracturing. SPE J. 25 (2), 573–586. https://doi.org/10.2118/199893-PA.

Wang, L., Chen, W., Vuik, C., 2022. Hybrid-dimensional modeling for fluid flow in heterogeneous porous media using dual fracture-pore model with flux interaction of fracture–cavity network. Gas Science and Engineering 100, 104450. https://doi.org/10.1016/j.jngse.2022.104450.

Wang, T., Chen, M., Wu, J., Lu, J.K., Luo, C., Chang, Z., 2021. Making complex fractures by re-fracturing with different plugging types in large stress difference reservoirs. J. Petrol. Sci. Eng. 201, 108413. https://doi.org/10.1016/j.petrol.2021.108413.

Wang, W.R., Zhang, G.Q., Zhao, C.Y., Shen, L.J., Chen, H.Z., Zhang, T.W., 2022. Stress interference between fractures of alternating fracturing of horizontal wells. In: The 56th U.S. Rock Mechanics/Geomechanics Symposium. https://doi.org/10.56952/ARMA-2022-0398.

Wang, W.X., Xian, C.G., Liang, X., Heng, W., Cheng, N., Wang, L.Z., 2017. Production controlling factors of the longmaxi shale gas formation: a case study of Huangjingba Shale Gas Field. In: SPE/IATMI Asia Pacific Oil & Gas Conference and Exhibition doi:10.2118/186874-MS.

Wang, Y., Zhao, X.B., Shang, J.L., Tang, C.Y., Deng, J.S., Xing, Y.Y., 2020. Novel technology to improve recovery of remaining oil in tight glutenite reservoir of

Junggar Basin: employing chemical diverting agents in refracturing operation. In: Abu Dhabi International Petroleum Exhibition & Conference. https://doi.org/10.2118/202641-MS.

Xie, J., Huang, H.Y., Ma, H.Y., Zeng, B., Tang, J.Z., Yu, W., Wu, K., 2018. Numerical investigation of effect of natural fractures on hydraulic-fracture propagation in unconventional reservoirs. J. Nat. Gas Sci. Eng. 54, 143–153. https://doi.org/10.1016/j.jngse.2018.04.006.

Yang, L., Sheng, X.C., Zhang, B., Yu, H.H., Wang, X.L., Wang, P., Mei, J., 2023. Propagation behavior of hydraulic fractures in shale under triaxial compression considering the influence of sandstone layers. Gas Science and Engineering 110, 204895. https://doi.org/10.1016/j.jgsce.2023.204895.

Yu, Y.P., Liu, J.X., Ma, X.L., Yang, G., Sun, Y.H., Sun, W.P., Shi, W.P., 2022. Mechanism analysis of multi-cluster fracture interference in horizontal wells of hydrate reservoirs in the South China Sea. Energy & Fuels 36 (7), 3580–3595. https://doi.org/10.1021/acs.energyfuels.2c00040.

Yuan, L.S., Zhou, F.J., Li, B., Gao, J.J., Yang, X.D., Cheng, J.Q., Wang, J., 2020. Experimental study on the effect of fracture surface morphology on plugging efficiency during temporary plugging and diverting fracturing. J. Nat. Gas Sci. Eng. 81, 103459. https://doi.org/10.1016/j.jngse.2020.103459.

Zhang, L.F., Zhou, F.J., Mou, J.Y., Pournik, M., Tao, S.D., Wang, D.B., Wang, Y.C., 2019. Large-scale true tri-axial fracturing experimental investigation on diversion behavior of fiber using 3D printing model of rock formation. J. Petrol. Sci. Eng. 181, 106171. https://doi.org/10.1016/j.petrol.2019.06.035.

Zhang, R.X., Hou, B., Tan, P., Muhadasi, Y., Fu, W.N., Dong, X.M., Chen, M., 2020. Hydraulic fracture propagation behavior and diversion characteristic in shale formation by temporary plugging fracturing. J. Petrol. Sci. Eng. 190, 107063. https://doi.org/10.1016/j.petrol.2020.107063.

Zhang, S.C., Li, S.H., Zou, Y.S., Li, J.M., Ma, X.F., Zhang, X.H., Wang, Z.F., Wu, S., 2021. Experimental study on fracture height propagation during multi-stage fracturing of horizontal wells in shale oil reservoirs. Journal of China University of Petroleum (Edition of Natural Science) 45 (1), 77–86 (in Chinese).

Zhang, Z.P., Zhang, S.C., Zou, Y.S., Ma, X.F., Li, N., Liu, L., 2021. Experimental investigation into simultaneous and sequential propagation of multiple closely spaced fractures in a horizontal well. J. Petrol. Sci. Eng. 202, 108531. https://doi.org/10.1016/j.petrol.2021.108531.

Zhu, H.Y., Huang, C.H., Tang, X.H., John, M., 2023. Multicluster fractures propagation during temporary plugging fracturing in naturally fractured reservoirs integrated with dynamic perforation erosion. SPE J. 28, 1986–2002. https://doi.org/10.2118/214666-PA.

Zou, Y.S., Ma, X.F., Zhang, S.C., Zhou, T., Li, H., 2016a. Numerical investigation into the influence of bedding plane on hydraulic fracture network propagation in shale formations. Rock Mech. Rock Eng. 49, 3597–3614. https://doi.org/10.1007/s00603-016-1001-5.

Zou, Y.S., Zhang, S.C., Zhou, T., Zhou, X., Guo, T.K., 2016b. Experimental investigation into hydraulic fracture network propagation in gas shales using CT scanning technology. Rock Mech. Rock Eng. 49, 33–45. https://doi.org/10.1007/s00603-015-0720-3.

Zou, Y.S., Ma, X.F., Zhou, T., Li, N., Chen, M., Li, S.H., Zhang, Y.N., Li, H., 2017. Hydraulic fracture growth in a layered formation based on fracturing experiments and discrete element modeling. Rock Mech. Rock Eng. 50, 2381–2395. https://doi.org/10.1007/s00603-017-1241-z.

Zou, Y.S., Ma, X.F., Zhang, S.C., 2020. Numerical modeling of fracture propagation during temporary-plugging fracturing. SPE J. 25 (3), 1503–1522. https://doi.org/10.2118/199351-PA.

Zou, Y.S., Shi, S.Z., Zhang, S.C., Yu, T.X., Tian, G., Ma, X.F., Zhang, Z.P., 2021. Experimental modeling of sanding fracturing and conductivity of propped fractures in conglomerate: a case study of Mahu tight conglomerate in Junggar Basin, China. Petrol. Explor. Dev. 48, 1202–1209 (in Chinese).

Zou, Y.S., Gao, B.D., Zhang, S.C., Ma, X.F., Sun, Z.Y., Wang, F., Liu, C.Y., 2022. Multi-fracture nonuniform initiation and vertical propagation behavior in thin interbedded tight sandstone: an experimental study. J. Petrol. Sci. Eng. 213, 110417. https://doi.org/10.1016/j.petrol.2022.110417.

Zou, Y.S., Li, Y.C., Yang, C., Zhang, S.C., Ma, X.F., Zou, L.Q., 2024. Fracture propagation law of temporary plugging and diversion fracturing in shale reservoirs under completion experiments of horizontal well with multi-cluster sand jetting perforation. Petrol. Explor. Dev. 51 (3), 624–634. https://doi.org/10.1016/S1876-3804(24)60500-8 (in Chinese).